The Astronomical Journal, 158:123 (17pp), 2019 September https://doi.org/10.3847/1538-3881/ab3211

Phase Curves from the Kuiper Belt: Photometric Properties of Distant Kuiper Belt Objects Observed by *New Horizons*

Anne J. Verbiscer[1], Simon Porter[2], Susan D. Benecchi[3], J. J. Kavelaars[4], Harold A. Weaver[5], John R. Spencer[2], Marc W. Buie[2], David Tholen[6], Bonnie J. Buratti[7], Paul Helfenstein[8], Alex H. Parker[2], Catherine B. Olkin[2], Joel Parker[2], S. Alan Stern[2], Leslie A. Young[2], Kimberly Ennico-Smith[9], Kelsi N. Singer[2], Andrew F. Cheng[5], and Carey M. Lisse[5]
The New Horizons Science Team

[1] University of Virginia, P.O. Box 400325, Charlottesville, VA 22904-4325, USA; verbiscer@virginia.edu
[2] Southwest Research Institute, Boulder, CO, USA
[3] Planetary Science Institute, Tucson, AZ, USA
[4] National Research Council of Canada, Victoria, BC, Canada
[5] The Johns Hopkins University Applied Physics Laboratory, Laurel, MD, USA
[6] University of Hawai'i, Honolulu, HI, USA
[7] Jet Propulsion Laboratory, Pasadena, CA, USA
[8] Cornell University, Ithaca, NY, USA
[9] NASA Ames Research Center, Moffett Field, CA, USA
Received 2019 May 14; revised 2019 July 9; accepted 2019 July 11; published 2019 August 23

Abstract

Prior to its close encounter with the Kuiper Belt object (KBO) (486958) 2014 MU_{69} on 2019 January 1, NASA's *New Horizons* spacecraft observed other KBOs from distances greater than 0.1 au at solar phase angles far larger than those attainable from Earth. The expanded range in phase angle afforded by these distant KBO (DKBO) observations enables comparisons between their phase functions and those of other solar system objects. Here we present extended *New Horizons* phase angle coverage of plutino (15810) Arawn (1994 JR_1) to 131°, resonant KBO 2012 HE_{85} to 64°, scattered disk KBO 2011 HK_{103} to 124°, hot classical (515977) 2012 HZ_{84} to 73°, and cold classical KBOs 2011 HJ_{103} and 2011 JY_{31} to 27° and 122°, respectively. In general, DKBO solar phase curves have slopes (i.e., phase coefficients) and shapes (with corresponding phase integrals q) similar to those of other dark, small solar system objects including comet nuclei, asteroids, and satellites. Until stellar occultations by these DKBOs provide information about their size, geometric albedos p (and Bond albedos $A = pq$) must be inferred from the median albedos measured by thermal radiometry for each dynamical class. Bond albedos for these DKBOs range from 0.01 to 0.04. Cold classical JY_{31} has a slightly lower slope and higher phase integral than the other DKBOs, and its slope and phase integral come closest to matching those of cold classical MU_{69}, suggesting that cold classical KBOs share surface scattering characteristics that are distinct from those of other KBOs.

Key words: Kuiper Belt objects: individual

1. Introduction

Photometric properties, such as the albedo and phase function, of airless planetary bodies can be derived from the quantitative measurement of reflected radiation from their surfaces at a variety of viewing geometries. Photometric models strive to infer physical surface properties such as roughness, porosity, particle structure and size from the analysis of the phase function, or the manner in which reflected light varies with illumination and viewing geometry. The success with which physical surface properties can be derived from photometric models depends highly on the availability of observations that span the full range of illumination and viewing geometries, from the lowest to the highest phase angles (Verbiscer & Helfenstein 1998). Observations at the lowest phase angles characterize the opposition effect, or surge, the dramatic, nonlinear increase in reflectance as phase angles approach zero near opposition. Reflectance measurements at large phase angles (e.g., $\alpha < 90°$) constrain physical surface characteristics such as the mean topographic slope, or roughness, while those at extreme phase angles, large and small, constrain the directional scattering behavior and particle transparency and opacity.

The size of Earth's orbit limits phase angle coverage for many solar system objects, even main belt asteroids, but spacecraft passing through the asteroid belt (e.g., *Galileo, Stardust, Deep Space 1*) and missions to asteroids (e.g., *Near Earth Asteroid Rendezvous–Shoemaker*, *NEAR Shoemaker*) have expanded phase angle coverage for asteroids and Jupiter family comets (JFCs), while outer solar system missions such as *Voyager*, *Galileo*, and *Cassini* have expanded the phase angle coverage for the icy satellites of the giant planets. Although Earth-based Kuiper Belt object (KBO) observations are limited to phase angles $\alpha < 2°$, the analysis of KBO phase curves near opposition has revealed correlations between the phase coefficient β, or slope of the phase curve, and dynamical class as well as wavelength dependences on β with dynamical class (e.g., Rabinowitz et al. 2007; Schaefer et al. 2009; Verbiscer et al. 2013).

In 2003, the National Research Council identified a Kuiper Belt/Pluto (KBP) mission as the highest medium class mission priority in its planetary science decadal survey (National Research Council Solar System Exploration Survey 2003). The goals of the KBP mission were to investigate the diversity of the physical and compositional properties of KBOs, perform a detailed reconnaissance of the Pluto/Charon system, and to assess the impact history of both large and small KBOs. Launched in 2006, NASA's *New Horizons* spacecraft performed that detailed reconnaissance of the Pluto/Charon system in 2015 July and assessed the impact history of those two large KBOs (Stern et al. 2015). Following a sequence of thruster burns to redirect the spacecraft trajectory in late 2015, NASA formally approved the *New Horizons* Kuiper Belt Extended Mission on 2016 July 1, and the spacecraft encountered the cold classical KBO (CCKBO) (486958) 2014 MU_{69} (hereafter MU_{69}) on 2019 January 1 (Moore et al. 2018; Stern et al. 2018, 2019) at a flyby distance of 3500 km and met many of the remaining goals of the KBP mission. As NASA's only observatory in the Kuiper Belt, *New Horizons* is exploring 18 other distant KBOs (DKBOs) as it flies through the outer solar system's circumstellar disk which contains some of its most primitive objects. The objectives of this exploration are fivefold:

1. measure light curves at multiple viewing geometries to determine KBO rotation rates, shapes, and pole positions;
2. construct solar phase curves to determine physical properties of DKBO regoliths;
3. use deep imaging to search for satellites and binaries smaller and closer than could be identified with current Earth-centric facilities;
4. search for ring and dust material around KBOs and Centaurs; and
5. measure astrometric positions to improve orbital solutions for future studies, including stellar occultations. The availability and precision of the *Gaia* catalog (Gaia Collaboration et al. 2018) now makes it possible to predict stellar occultations by small DKBOs, including MU_{69} (Buie et al. 2019), with sufficient accuracy that the likelihood of success is high enough to justify deployments to remote locations.

Now from its unique vantage point in the outer solar system, *New Horizons'* observes KBOs at nearly the full range of solar phase angles, with its viewing geometry limited only by flight rules that prohibit pointing close to the Sun, e.g., at $\alpha > 165°$.

In companion papers, S. B. Porter et al. (2019, in preparation) present light curves and astrometry for the DKBOs observed by *New Horizons* in 2017, and A. H. Parker et al. (2019, in preparation) discuss the techniques and results from searches for ring and dust material around DKBOs. Searches for smaller satellites and close binaries with deep imaging must await downlinks of unbinned images with the highest spatial resolution from the spacecraft following the MU_{69} encounter.

Here we present solar phase curves of six long-range KBO targets observed by *New Horizons* from five dynamical classes: one plutino, one resonant KBO, one KBO from the scattered disk, and three classical KBOs (one hot and two cold). In subsequent papers we will present phase curves from dwarf planets observed by *New Horizons* as well as additional distant KBOs observed after 2018 September. Five of these DKBOs were discovered by the *New Horizons* search team during a ground-based campaign to find a KBO flyby target for the spacecraft to visit after the Pluto flyby in 2015. This work includes a reanalysis of the phase curve of plutino (15810) Arawn (1994 JR_1; Porter et al. 2016) using all available Earth-based low phase angle observations and additional high phase angle observations not included by Porter et al. (2016). The analyses of these CCKBO solar phase curves provide our only knowledge of the photometric properties of CCKBOs as a class to place the observations from the close flyby of CCKBO MU_{69} in context.

2. Observations

New Horizons' Long-range Reconnaissance Imager (LORRI; Cheng et al. 2008) is the instrument used to investigate the photometric properties of distant KBOs. Mounted in a fixed position on the *New Horizons* spacecraft, LORRI is a 20.8 cm aperture, $f/12.6$ Ritchey–Chretien optical telescope with a $0\overset{\circ}{.}29$ (1044″) field of view, coupled with a back-illuminated CCD with 1024×1024 illuminated pixels. LORRI has no filters and its bandpass extends from 350 to 850 nm, with a pivot wavelength at 601 nm. LORRI's native pixel resolution is 1″/pixel, however, the observations presented here were all binned 4×4 to 256×256 pixels, producing 4″/pixel images. *New Horizons* does not have reaction wheels, thus all pointing must be done with thrusters. The spacecraft thrusters are generally able to maintain pointing stability within about $3\overset{''}{.}5$; therefore, 4×4 images are only slightly reduced in actual resolution compared to the resolution of 1×1 images. Binned images also require far less data volume than unbinned images, reducing the downlink time from the spacecraft which is now at a light-travel time of more than 6 hr from Earth.

Before 2017 December, all distant KBO LORRI observations used an exposure time of 10 s. However, a few experimental images taken in 2017 September demonstrated that the spacecraft has sufficient attitude stability to permit LORRI observations using exposure times as long as 30 s. Beginning in 2017 December, all long-range KBO images were acquired using 30 s exposures, improving the sensitivity of LORRI by a factor of $2 \sim 3$ compared to previous limits using 10 s exposures. The sensitivity of LORRI is such that distant KBOs must also have apparent magnitude $V < 21$ in order to be detected. Typically, long-range KBO LORRI observations consist of sequences, or visits, of exposures at a fixed R.A.–decl. pointing. The number of images in each visit varies depending on the brightness of the KBO, and, as of 2017 December, each visit requires fewer 30 s exposures to match or exceed the signal-to-noise ratio achieved previously using 10 s exposures. Without a dense background star field and viewing at solar elongations >40°, the limiting magnitude of 10 s and 30 s LORRI exposures is $V \approx 20$ and $V \approx 21$, respectively. The image reduction techniques used here are explained in detail in a companion paper by S. B. Porter et al. (2019, in preparation) and in Porter et al. (2018). The reduction pipeline is an updated version of the one used in the first analysis of LORRI images of (15810) Arawn (1994 JR_1), as described in Porter et al. (2016).

The data number per second (DN/s) fluxes convert approximately to a Johnson *V* magnitude (recall that LORRI is an unfiltered CCD) using the same equation as in Porter et al. (2016),

$$V_{\mathrm{LORRI}} = -2.5 \log_{10}(\mathrm{DN/s}) + 18.94 + \mathrm{CC}, \qquad (1)$$

where CC is a color correction as described below and in detail for each DKBO. This equation includes the appropriate zero-point correction ($V = 18.94$) for the LORRI 4×4 images, calibrated with images of the well-characterized open cluster M7/NGC 6475 (H. A. Weaver et al. 2019, in preparation). To determine the color correction CC for each KBO, we use the Space Telescope Data Analysis System (STDAS) synthetic photometry (synphot) software package provided by the Space Telescope Science Institute (STScI; Laidler et al. 2005) to

Table 1
Earth-based Observations of Plutino (15810) Arawn (1994 JR_1)

Observation Mid-time	r (au)	Δ (au)	α (°)	Filter	Magnitude	V Magnitude at 1 au	Telescope/Observatory	References
1994 May 15 00:58	34.765	33.767	0.311	V	22.8	7.4	Isaac Newton/La Palma	(1), (2)
1995 Mar 29 17:14	34.757	34.219	1.402	R	22.19 ± 0.04	7.57	Isaac Newton/La Palma	(3)
1995 Mar 29 18:35	34.757	34.218	1.401	R	22.18 ± 0.04	7.56	Isaac Newton/La Palma	(3)
1995 Mar 30 17:51	34.757	34.204	1.386	R	22.30 ± 0.07	7.68	Isaac Newton/La Palma	(3)
1995 Mar 30 18:15	34.757	34.204	1.386	V	23.05 ± 0.05	7.67	Isaac Newton/La Palma	(3)
2001 Jul 28 02:49	34.800	34.131	1.266	F555W	22.84 ± 0.05	7.47	WFPC2/*HST*	(4)
2015 Jun 12 13:20	35.436	34.493	0.617	R	22.0 ± 0.05	7.3	2.24 m/Univ. Hawaii	(5)
2015 Jun 12 13:56	35.436	34.493	0.617	R	22.1 ± 0.05	7.4	2.24 m/Univ. Hawaii	(5)
2015 Nov 2 05:45	35.464	35.913	1.423	F606W	23.00 ± 0.03	7.48	WFC3/*HST*	(6), (7)

References. (1) MPS 23646, (2) Irwin et al. (1995), (3) Green et al. (1997), (4) Benecchi et al. (2011), (5) MPS 610233, (6) Porter et al. (2016), (7) Benecchi et al. (2019).

Table 2
LORRI Observations of Plutino (15810) Arawn (1994 JR_1)

Observation Mid-time	r (au)	Δ (au)	α (°)	Exposure Time (s)	Total Images	LORRI Magnitude	V Magnitude at 1 au[a]
2015 Nov 2 12:46	35.464	1.847	26.725	9.967	10	17.795 ± 0.019	8.927
2015 Nov 2 13:46	35.464	1.847	26.728	9.967	10	17.905 ± 0.017	9.037
2015 Nov 2 14:46	35.464	1.846	26.731	9.967	10	17.786 ± 0.017	8.919
2015 Nov 2 15:46	35.464	1.846	26.734	9.967	10	17.811 ± 0.019	8.944
2016 Apr 7 19:02	35.494	0.711	58.480	9.967	24	17.132 ± 0.008	10.335
2016 Apr 7 19:32	35.494	0.711	58.491	9.967	24	17.296 ± 0.007	10.499
2016 Apr 7 20:30	35.494	0.711	58.511	9.967	3	16.731 ± 0.007	9.934
2016 Apr 7 21:00	35.494	0.711	58.521	9.967	3	16.740 ± 0.008	9.943
2016 Apr 7 21:30	35.494	0.711	58.531	9.967	3	16.905 ± 0.009	10.108
2016 Apr 7 22:00	35.494	0.711	58.542	9.967	3	17.085 ± 0.008	10.288
2016 Apr 7 22:30	35.494	0.710	58.552	9.967	3	17.101 ± 0.011	10.307
2016 Apr 7 23:00	35.494	0.710	58.562	9.967	3	16.739 ± 0.010	9.945
2016 Apr 7 23:30	35.494	0.710	58.572	9.967	3	16.835 ± 0.006	10.041
2016 Apr 8 00:00	35.494	0.710	58.583	9.967	3	16.680 ± 0.007	9.886
2016 Apr 8 00:30	35.494	0.710	58.593	9.967	3	16.977 ± 0.011	10.183
2016 Apr 8 01:30	35.494	0.710	58.614	9.967	3	17.114 ± 0.010	10.320
2016 Apr 8 02:30	35.494	0.710	58.634	9.967	3	16.707 ± 0.007	9.913
2016 Apr 8 03:30	35.494	0.709	58.655	9.967	3	17.041 ± 0.009	10.250
2016 Apr 8 04:30	35.494	0.709	58.676	9.967	3	17.007 ± 0.010	10.216
2016 Apr 8 05:30	35.494	0.709	58.696	9.967	3	16.772 ± 0.008	9.981
2016 Apr 8 06:30	35.494	0.709	58.717	9.967	3	17.186 ± 0.009	10.395
2016 Apr 8 07:30	35.494	0.708	58.738	9.967	3	16.699 ± 0.007	9.911
2016 Apr 8 08:30	35.494	0.708	58.759	9.967	3	16.835 ± 0.008	10.047
2016 Apr 8 09:30	35.494	0.708	58.779	9.967	3	17.350 ± 0.013	10.562
2016 Jul 13 05:32	35.513	0.621	130.762	9.967	30	19.017 ± 0.077	12.513
2016 Jul 13 06:32	35.513	0.621	130.789	9.967	30	18.612 ± 0.033	12.108

Note.
[a] Color correction applied to transform LORRI magnitudes to Johnson V is +0.213 mag, using Arawn's color from Porter et al. (2016).

transform all Earth-based observations to the Johnson V-magnitude system using the colors of each DKBO classification provided by Hainaut et al. (2012).

All of the Earth-based, low phase angle observations of the six DKBOs presented herein are only sparsely sampled during the period between 1994 and 2017 at phase angles ranging from $\alpha = 0\overset{\circ}{.}059$ to $\alpha = 1\overset{\circ}{.}45$. They provide some low-phase, near-opposition information for each DKBO's phase curve but have insufficient sampling to characterize their rotational light curves at small phase angles. Future ground-based observations of all *New Horizons* DKBOs acquired at a high cadence (sampling several times over the rotation period) will provide near-opposition photometry, reduce uncertainties in the rotation period, and contribute to the determination of their rotation poles and shapes.

2.1. Plutino (15810) Arawn (1994 JR_1)

(15810) Arawn (1994 JR_1) was discovered with the Isaac Newton Telescope at the Roque de los Muchachos Observatory (Irwin et al. 1995) in 1994. In a 3:2 mean-motion resonance with Neptune, Arawn is therefore classified as a plutino. Low phase angle, ground-based observations of Arawn include

Table 3
Earth-based Observations of Resonant KBO 2012 HE_{85}

Observation Mid-time	r (au)	Δ (au)	α (°)	Instrument	Filter	Total Observations	Magnitude	V Magnitude at 1 au
2012 Apr 18 08:06	40.165	39.814	1.353	Megacam[a]	open,r	1	25.588 ± 0.051	9.885
2012 Apr 19 07:25	40.165	39.799	1.346	Megacam	open,r	3	25.093 ± 0.108	9.390
2013 Jun 8 04:39	40.176	39.234	0.554	Megacam	open,gr	2	25.282 ± 0.048	9.293
2013 Jun 11 06:47	40.176	39.215	0.483	Megacam	open,gr	3	25.357 ± 0.078	9.370
2013 Jun 13 05:12	40.176	39.204	0.439	Megacam	open,gr	1	24.408 ± 0.096	8.422
2016 Jun 5 12:37	40.219	39.333	0.703	HSC[b]	r	7	25.049 ± 0.072	9.369
2016 Jul 5 14:39	40.221	39.206	0.059	WFC3/UVIS[c]	F606W	2	24.80 ± 0.05	8.81
2017 Jul 20 10:58	40.241	39.254	0.330	HSC	$r2$	8	24.738 ± 0.046	9.061
2017 Jul 21 08:39	40.241	39.258	0.352	HSC	$r2$	2	24.535 ± 0.042	8.858

Notes.
[a] Megacam (McLeod et al. 2015) on the Magellan telescopes at Las Campanas Observatory, Chile.
[b] Hyper Suprime-Cam (Miyazaki et al. 2012) on the National Astronomical Observatory of Japan's Subaru Telescope at Maunakea Observatory, Hawaii.
[c] *HST* (Benecchi et al. 2019).

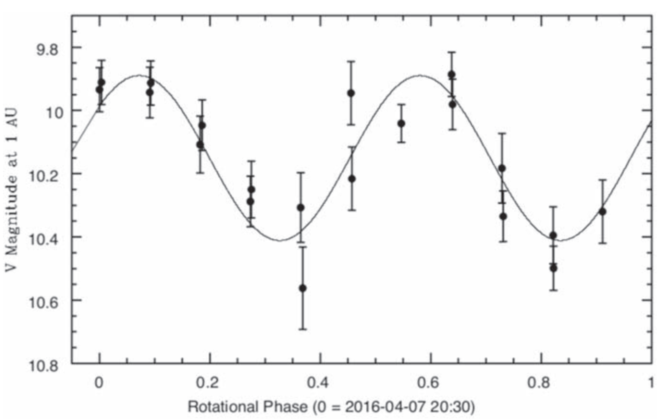

Figure 1. Updated rotation curve of Plutino (15810) Arawn (JR_1) assembled using all *New Horizons* LORRI observations acquired in 2016 April listed in Table 2 phase folded over a period of 5.49 hr with median V magnitude at 1 au 10.15. Solid line is a one-term Fourier fit to the $\alpha = 58°$ data (black circles) with a peak-to-peak amplitude 0.5 mag. Observations are phased to 2016 April 7 20:30.

those made by Green et al. (1997) in V and R and by D. Tholen in R 2015 June (MPS 610223). The *Hubble Space Telescope* (*HST*) observed Arawn in 2001 using *HST*/WFPC2 (Benecchi et al. 2011) and in 2015 using *HST*/WFC3 (Porter et al. 2016; Benecchi et al. 2019). Table 1 summarizes the Earth-based, low phase angle observations of Arawn. Table 2 summarizes all of the *New Horizons* LORRI observations of Arawn, including additional high phase angle observations (at $\alpha = 131°$) not included in the Porter et al. (2016) analysis. All LORRI photometry reported in Table 2 use the updated reduction pipeline described by S. B. Porter et al. (2019, in preparation). This updated reduction pipeline improved the photometric results significantly, reducing the uncertainty in each measurement reported by Porter et al. (2016) by at least an order of magnitude. Here we present a reanalysis of *New Horizons* (15810) Arawn photometry using these updated reduction techniques and all available observations from $\alpha = 0\overset{\circ}{.}3$ to 131°.

The rotation curve for Arawn (Figure 1) now includes the improved photometry from S. B. Porter et al. (2019, in preparation), has a peak-to-peak amplitude of 0.5 mag, and shows that Arawn's rotation period is 5.49 hr. Although the period is close to that measured by Porter et al. (2016; 5.47 hr), the shape of the light curve has changed as a result of using the improved photometry, despite the fact that both light curves are phased to the same time (2016 April 7 20:30 UT). The updated light-curve maxima now approximately coincide with the previous light-curve minima. Light-curve maxima now occur at rotation phases 0.1 and 0.7, where they had previously occurred at rotation phases 0.33 and 0.85; light-curve minima are now at rotation phase 0.36 and 0.8, and they had been at rotation phases 0.1 and 0.6. The total amplitude of the updated light curve (0.5 mag) at $\alpha = 58°$ is not as large as the previously measured amplitude (0.8 mag). The rotation period is well within the 3.56–12 hr range measured for 29 KBOs and Centaurs by Thirouin et al. (2010), but slightly faster than the average 7.5 hr period found for their sample. The 0.5 mag amplitude is higher than the 0.1 mag average amplitude found by Thirouin et al. (2010) for their sample; however, the phase angle at which the LORRI rotation curve was measured ($\alpha = 58°$) is much larger than phase angles at which the 29 objects in the Thirouin et al. (2010) study were observed. The highest phase angle at which the KBOs and Centaur light curves were measured in the Thirouin et al. (2010) study was $\alpha = 10°$.

Saturn's irregular satellites are thought to be captured KBOs (Jewitt & Haghighipour 2007) and have rotational light curves that increase in amplitude, by as much as 2.5 mag, with increasing phase angle (Denk & Mottola 2019); therefore, the 0.5 mag variation observed in Arawn's light curve measured at $\alpha = 58°$ is consistent with the 0.25 mag variation in the low-phase, Earth-based observations of Arawn. *New Horizons* LORRI observed Arawn twice at $\alpha = 131°$ in 2016 July (Table 2). Using Arawn's 5.49 hr period and light curve acquired in 2016 April, just 100 days earlier, indicates that Arawn was at a light-curve mean at UT 05:32 on 2016 July 13 and a light-curve maximum just one hour later at UT 06:32. Therefore, we apply a 1.25 mag correction to the LORRI observation of Arawn acquired at the light-curve maximum at UT 06:32 on 2016 July 13, since all of the saturnian irregular satellites studied by Denk & Mottola (2019) at phase angles $\alpha > 100°$ have total light-curve amplitudes of ~2.5 mag. We apply no correction to the observation acquired at the light-curve mean at UT 05:32. With only two observations, however, we do not know the actual amplitude of Arawn's light curve at $\alpha = 131°$, but given the results of the Denk & Mottola (2019)

Table 4
LORRI Observations of Resonant KBO 2012 HE_{85}

Observation Mid-time	r (au)	Δ (au)	α (°)	Exposure Time (s)	Total Images	LORRI Magnitude	V Magnitude at 1 au[a]
2017 Sep 22 19:40	40.244	0.796	19.608	9.967	4	17.531 ± 0.029	10.250
2017 Sep 22 21:10	40.244	0.796	19.621	9.967	4	17.724 ± 0.040	10.443
2017 Sep 22 22:40	40.244	0.796	19.634	9.967	4	17.790 ± 0.040	10.512
2017 Sep 23 04:40	40.244	0.793	19.685	9.967	4	18.067 ± 0.046	10.794
2017 Sep 23 07:40	40.244	0.792	19.711	9.967	4	17.725 ± 0.031	10.455
2017 Sep 23 09:10	40.244	0.792	19.723	9.967	4	17.891 ± 0.044	10.621
2017 Sep 23 10:40	40.244	0.791	19.736	9.967	4	17.703 ± 0.028	10.436
2017 Sep 23 15:10	40.244	0.790	19.775	9.967	4	17.718 ± 0.052	10.453
2017 Sep 23 21:10	40.244	0.788	19.827	9.967	4	17.907 ± 0.028	10.648
2017 Nov 2 11:30	40.247	0.507	33.730	9.967	4	17.143 ± 0.011	10.841
2017 Nov 2 13:00	40.247	0.506	33.777	9.967	4	17.205 ± 0.012	10.906
2017 Nov 2 14:30	40.247	0.506	33.800	9.967	4	17.270 ± 0.013	10.973
2017 Nov 2 16:00	40.247	0.506	33.836	9.967	4	17.301 ± 0.011	11.004
2017 Nov 2 17:30	40.247	0.505	33.871	9.967	4	17.334 ± 0.014	11.041
2017 Nov 2 19:00	40.247	0.505	33.906	9.967	4	17.032 ± 0.010	10.739
2017 Nov 2 20:30	40.247	0.504	33.942	9.967	4	17.079 ± 0.013	10.790
2017 Nov 2 22:00	40.247	0.504	33.978	9.967	4	17.195 ± 0.011	10.906
2017 Nov 2 23:30	40.247	0.504	34.013	9.967	4	17.327 ± 0.017	11.038
2017 Nov 3 01:00	40.247	0.504	34.048	9.967	4	17.270 ± 0.009	10.985
2017 Nov 3 02:30	40.247	0.503	34.084	9.967	4	17.353 ± 0.015	11.068
2017 Nov 3 04:00	40.247	0.502	34.119	9.967	4	17.397 ± 0.016	11.117
2017 Nov 3 05:30	40.247	0.502	34.155	9.967	4	17.212 ± 0.010	10.932
2017 Nov 3 07:00	40.247	0.502	34.191	9.967	4	17.244 ± 0.013	10.964
2017 Nov 3 08:30	40.247	0.501	34.226	9.967	4	17.222 ± 0.015	10.946
2017 Nov 3 10:00	40.247	0.501	34.263	9.967	4	17.281 ± 0.013	11.005
2017 Nov 3 11:30	40.247	0.500	34.299	9.967	4	17.340 ± 0.016	11.068
2017 Nov 3 13:00	40.247	0.500	34.335	9.967	4	17.143 ± 0.009	10.871
2017 Dec 5 09:36	40.249	0.342	62.980	29.967	4	17.509 ± 0.009	12.062
2017 Dec 6 09:51	40.249	0.341	64.271	29.967	4	17.362 ± 0.008	11.921

Note.
[a] Color correction applied to transform LORRI magnitudes to Johnson V is +0.247 mag, using color from Benecchi et al. (2019) and the average color for resonant objects measured by Hainaut et al. (2012).

study, the amplitude of Arawn's light curve at this high phase angle is almost certainly greater than its amplitude at $\alpha = 58°$ and may be as high as that of the saturnian satellites at $\alpha > 100°$. In the absence of a complete light curve for Arawn at $\alpha = 131°$, applying a light-curve correction based on the average amplitude of saturnian irregular satellites at high phase angles is more appropriate than forgoing any light-curve correction at all.

2.2. *Resonant KBO 2012 HE_{85}*

First observed on 2012 April 18, 2012 HE_{85} (hereafter HE_{85}) was discovered by the *New Horizons* KBO search team using the Magellan II (Clay) telescope at Las Campanas Observatory in Chile (MPEC 2016:B36). As it is in a 9:5 mean-motion resonance with Neptune, it is classified as a resonant KBO. Table 3 summarizes Earth-based observations of HE_{85} acquired from Magellan, Subaru, and *HST* from 2012 to 2017. These low phase angle observations are only sparsely sampled over a five year period at phase angles ranging from $\alpha = 0\overset{\circ}{.}059$ to $\alpha = 1\overset{\circ}{.}35$.

New Horizons LORRI observed HE_{85} at three epochs in 2017: UT September 21, November 2, and December 6, at distances of 0.8, 0.5, and 0.3 au, respectively. Table 4 summarizes the HE_{85} LORRI observations and photometry. Among the KBOs observed by *New Horizons* in 2017, the observations of HE_{85} had the highest signal-to-noise ratio, and at the time they were acquired, the December observations at 0.3 au were the closest observations of a KBO other than Pluto, although *New Horizons* later observed KBOs from even closer ranges in 2018 and 2019. The September and November epochs were intended to be light-curve sequences of 72 10 s images spread over 25.5 hr, in 18 visits consisting of four images each, at phase angles of ~20° and 34°. However, in addition to being fainter because they were acquired at greater distances, the September HE_{85} observations also had an extremely high background star density, and several images had to be discarded because HE_{85} was adjacent to a star that saturated LORRI and thus could not be subtracted. Therefore, the September observation sampling was not sufficient to constrain the rotation period of HE_{85} and only images from the November visit could be used. While the images acquired during the November visit still had a high star density, the density was not as high as September's and images from all 18 visits contribute to the rotational light curve of HE_{85}. From applying a Fourier fit to the $\alpha = 34°$ data from November only, HE_{85} has a 18.8784 hr period, and the double-peaked rotational light curve (Figure 2) has a total amplitude of 0.4 mag. In December, LORRI made four visits consisting of four 30 s images spread over 18 hr at a phase angle of ~64°; however, two of the four visits had to be discarded because of nearby

Table 5
Earth-based Observations of Hot Classical KBO (516977) 2012 HZ_{84}

Observation Mid-time	r (au)	Δ (au)	α (°)	Instrument	Filter	Total Observations	Magnitude	V Magnitude at 1 au
2011 Apr 28 08:19	41.331	40.818	1.214	Megacam[a]	emp,r	2	25.797 ± 0.085	9.661
2011 May 4 08:48	41.328	40.728	1.137	Megacam	emp,r	1	25.498 ± 0.083	9.367
2012 Apr 17 08:57	41.166	40.833	1.329	Megacam	emp,r	1	26.054 ± 0.104	9.926
2012 Apr 19 09:02	41.165	40.800	1.313	Megacam	open,r	1	25.971 ± 0.085	9.845
2013 Jun 13 08:28	40.972	40.000	0.428	Megacam	open,gr	1	25.820 ± 0.089	9.747
2014 Jun 25 11:10	40.801	39.792	0.187	HSC[b]	r	14	25.663 ± 0.035	9.611
2014 Jun 27 09:01	40.800	39.787	0.144	HSC	r	4	24.882 ± 0.047	8.830
2017 Jul 20 09:57	40.306	39.320	0.331	HSC	$r2$	11	25.161 ± 0.086	9.161
2017 Jul 21 09:03	40.306	39.323	0.354	HSC	$r2$	7	25.273 ± 0.137	9.273

Notes.
[a] Megacam (McLeod et al. 2015) on the Magellan telescopes at Las Campanas Observatory, Chile.
[b] Hyper Suprime-Cam (Miyazaki et al. 2012) on the National Astronomical Observatory of Japan's Subaru Telescope at Maunakea Observatory, Hawaii.

bright stars, despite the lower star density of all HE_{85} epochs. While the December observations were obtained at higher phase angles than the ones in September and November, the range was small enough that their signal-to-noise ratios were comparable to the November observations, and roughly double those of the September observations. Figure 2 includes the December observations phase folded with the 18.8784 hr period, but neither they nor the September observations contributed to measuring the period owing to the paucity of data points at each epoch.

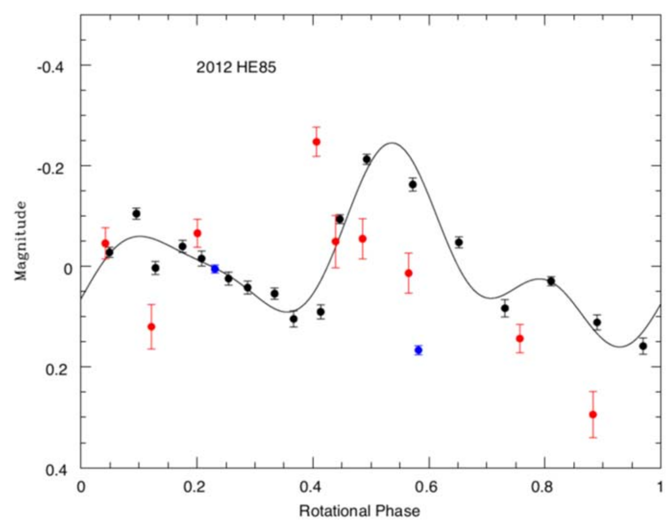

Figure 2. Rotation curve of resonant KBO HE_{85} from *New Horizons* LORRI observations acquired at three different epochs in 2017 September, November, and December (Table 4). Observations are phased to UT 2017 September 22 12:00. Solid curve is a four-term Fourier fit to the $\alpha = 34°$ data (black circles) with a total amplitude of 0.4 mag and a 18.8784 hr period. Data at $\alpha = 20°$ (red circles) and $\alpha = 64°$ (blue circles) are scaled to the reflectance at $\alpha = 34°$ using the solar phase function of 2012 HE_{85} (Figure 5). These data were not used to determine the rotation period because neither epoch had sufficient sampling; they are merely plotted on the curve using the rotation period from the fit to the $\alpha = 34°$ data. See the text for details.

2.3. Hot Classical KBO (516977) 2012 HZ_{84}

Like HE_{85}, (516977) 2012 HZ_{84} (hereafter HZ_{84}) was also discovered by the *New Horizons* KBO search team using the Magellan II (Clay) telescope at Las Campanas Observatory in Chile (MPS 505439). Earth-based observations of this hot classical KBO acquired from Magellan and Subaru from 2011 to 2017 are summarized in Table 5. These low phase angle observations are only sparsely sampled over a six year period at phase angles ranging from $\alpha = 0.°14$ to $\alpha = 1.°33$.

New Horizons observed HZ_{84} at the same three epochs in 2017 as HE_{85} (UT September 21, November 2, and December 6) at slightly larger phase angles (29°, 46°, and 73°) and distances (0.9, 0.6, and 0.5 au). Due to the larger distances and higher phase angles, HZ_{84} appeared dimmer than HE_{85}, and therefore *New Horizons* obtained no light-curve observations of HZ_{84}. At each epoch, LORRI acquired 25 images during three visits separated by 30–85 minutes. However, like HE_{85}, bright stars interfered with HZ_{84} in three of the nine visits, necessitating rejection of these images, so there are two visits from September, one from November, and three from December. Table 6 summarizes the LORRI HZ_{84} observations and photometry.

2.4. CCKBO 2011 HJ_{103}

Earth-based observations of the CCKBO 2011 HJ_{103} (hereafter HJ_{103}) acquired from Magellan and Subaru from 2011 to 2017 are summarized in Table 7. These low phase angle observations are only sparsely sampled over a six year period at phase angles ranging from $\alpha = 0.°20$ to $\alpha = 1.°24$.

New Horizons planned to observe HJ_{103} using a similar sequence as 2012 HE_{85}, with 18 light curve visits in September and four visits in November and December. However, ground-based observations of 2011 HJ_{103} were sparse, and the most recent ground-based observation used to target the *New Horizons* visits was a Gemini program that had incorrect timing information in its headers. This error resulted in a significant offset between where LORRI was pointed and the actual location of HJ_{103}. Fortunately, LORRI did catch HJ_{103} at the edge of its CCD in five of the September 18 visits (Table 8). LORRI also captured HJ_{103} in its field of view during a sixth visit, but the KBO was obscured by a star. The erroneous orbit was only discovered in mid-2017 November and not in time to correct the commanding for the visits in November and December. Unfortunately, HJ_{103} was fully off the LORRI CCD for the November and December observations. Therefore the LORRI observations in Table 8 only provide visits at a single phase angle, $\alpha = 27°$.

Table 6
LORRI Observations of Hot Classical KBO (516977) 2012 HZ_{84}

Observation Mid-time	r (au)	Δ (au)	α (°)	Exposure Time (s)	Total Images	LORRI Magnitude	V Magnitude at 1 au[a]
2017 Sep 17 13:02	40.280	0.938	28.758	9.967	25	19.465 ± 0.119	11.810
2017 Sep 17 14:02	40.280	0.938	28.768	9.967	25	18.890 ± 0.056	11.235
2017 Nov 2 03:02	40.261	0.637	46.329	9.967	25	18.933 ± 0.051	12.119
2017 Dec 6 11:16	40.246	0.500	73.004	29.967	25	19.256 ± 0.021	12.969
2017 Dec 6 12:41	40.246	0.500	73.060	29.967	25	19.326 ± 0.023	13.039
2017 Dec 6 13:41	40.246	0.499	73.100	29.967	25	19.173 ± 0.027	12.890

Note.
[a] Color correction applied to transform LORRI magnitudes to Johnson V is +0.231 mag, using the average color for hot classical KBOs measured by Hainaut et al. (2012).

Table 7
Earth-based Observations of CCKBO 2012 HJ_{103}

Observation Mid-time	r (au)	Δ (au)	α (°)	Instrument	Filter	Total Observations	Magnitude	V Magnitude at 1 au
2011 Apr 28 07:39	40.614	40.105	1.238	Megacam[a]	emp,r	2	24.922 ± 0.043	8.862
2011 Apr 30 09:30	40.614	40.074	1.213	Megacam	emp,r	1	25.274 ± 0.178	9.216
2011 May 6 08:51	40.612	39.988	1.132	Megacam	emp,r	1	25.134 ± 0.128	9.081
2011 May 31 10:31	40.606	39.707	0.674	Megacam	emp,r	1	23.633 ± 0.100	7.596
2011 Jun 4 07:06	40.605	39.677	0.591	Megacam	emp,r	1	24.355 ± 0.105	8.319
2014 Jun 25 11:01	40.334	39.325	0.199	HSC[b]	r	16	23.889 ± 0.025	7.887
2016 Jun 5 12:08	40.177	39.294	0.712	HSC	r	10	24.560 ± 0.059	8.568
2017 Jul 20 10:21	40.092	39.103	0.318	HSC	$r2$	11	24.165 ± 0.056	8.188
2017 Jul 21 09:49	40.091	39.106	0.341	HSC	$r2$	3	24.897 ± 0.127	8.921

Notes.
[a] Megacam (McLeod et al. 2015) on the Magellan telescopes at Las Campanas Observatory, Chile.
[b] Hyper Suprime-Cam (Miyazaki et al. 2012) on the National Astronomical Observatory of Japan's Subaru Telescope at Maunakea Observatory, Hawaii.

Table 8
LORRI Observations of CCKBO 2011 HJ_{103}

Observation Mid-time	r (au)	Δ (au)	α (°)	Exposure Time (s)	Total Images	LORRI Magnitude	V Magnitude at 1 au[a]
2017 Sep 20 15:30	40.079	0.674	26.671	9.967	4	17.240 ± 0.014	10.523
2017 Sep 20 17:00	40.079	0.674	26.700	9.967	4	17.178 ± 0.010	10.461
2017 Sep 20 20:00	40.079	0.673	26.757	9.967	4	17.089 ± 0.010	10.375
2017 Sep 21 03:30	40.079	0.671	26.902	9.967	4	16.978 ± 0.008	10.271
2017 Sep 21 08:00	40.079	0.670	26.990	9.967	4	17.279 ± 0.008	10.575

Note.
[a] Color correction applied to transform LORRI magnitudes to Johnson V is +0.441 mag, using the average color for CCKBOs measured by Hainaut et al. (2012).

2.5. Scattered Disk Object 2011 HK_{103}

Earth-based observations of the scattered disk KBO 2011 HK_{103} (hereafter HK_{103}) acquired from Subaru and *HST* from 2014 to 2017 are summarized in Table 9. These low phase angle observations were acquired over a narrow range of phase angles between $\alpha = 0.^\circ 13$ and $\alpha = 0.^\circ 65$.

New Horizons observed HK_{103} shortly after the spacecraft returned to three-axis mode in 2018 August and LORRI acquired observations in three epochs with 18 visits each (Table 10). The first epoch in 2018 August acquired one image in each of the 18 visits at $\alpha = 51°$ at time intervals ranging from 30 minutes to 2 hr apart. The second epoch on 2018 September 10 acquired two images in each of the 18 visits at $\alpha = 96°$ at time intervals ranging from one to three hours apart. The third epoch on 2018 September 28 acquired 10 images in each of the nine visits at $\alpha = 124°$ with 30 s exposures to increase signal-to-noise ratios, but HK_{103} was only detectable in stacks of the 10 images in three of those visits.

The rotational light curve of HK_{103} from the *New Horizons* LORRI data (Figure 3) demonstrates clearly that the amplitude of HK_{103}'s light curve increases with increasing phase angle, just as Denk & Mottola (2019) found for the irregular satellites of Saturn. A Lomb-Scargle periodogram analysis (Lomb 1976; Scargle 1982) of the observations acquired at $\alpha = 51°$ yields a statistically significant period of 10.83012 hr for HK_{103}. A three-term Fourier fit to the $\alpha = 51°$ data folded onto a rotation period of 10.83012 hr yields a double-peaked light curve with a total amplitude 0.2 mag. A three-term Fourier fit to the $\alpha = 96°$ data folded onto the same rotation period yields a double-peaked

Table 9
Earth-based Observations of Scattered Disk KBO 2011 HK_{103}

Observation Mid-time	r (au)	Δ (au)	α (°)	Instrument	Filter	Total Images	Magnitude	V Magnitude at 1 au
2014 Jun 25 10:53	43.425	42.415	0.171	HSC[a]	r	18	23.775 ± 0.017	7.727
2014 Jun 27 09:18	43.424	42.410	0.131	HSC	r	2	23.329 ± 0.014	7.281
2016 Jun 5 12:46	42.914	42.024	0.646	HSC	r	13	23.715 ± 0.026	7.713
2016 Jun 18 14:41	42.91	41.93	0.38	WFC3/*HST*[b]	F606W	2	23.98 ± 0.03	7.705
2017 Jul 20 11:02	42.624	41.640	0.324	HSC	$r2$	17	23.603 ± 0.021	7.636
2017 Jul 21 09:33	42.623	41.643	0.345	HSC	$r2$	26	23.619 ± 0.0347	7.652

Notes.
[a] Hyper Suprime-Cam (Miyazaki et al. 2012) on the National Astronomical Observatory of Japan's Subaru Telescope at Maunakea Observatory, Hawaii.
[b] Benecchi et al. (2019).

Table 10
LORRI Observations of Scattered Disk KBO 2011 HK_{103}

Observation Mid-time	r (au)	Δ (au)	α (°)	Exposure Time (s)	Total Images	LORRI Magnitude	V Magnitude at 1 au[a]
2018 Aug 17 08:00	42.349	0.291	50.279	9.967	1	15.578 ± 0.060	10.346
2018 Aug 17 09:00	42.349	0.291	50.339	9.967	1	15.760 ± 0.099	10.528
2018 Aug 17 10:00	42.349	0.291	50.400	9.967	1	15.690 ± 0.063	10.458
2018 Aug 17 12:00	42.349	0.290	50.522	9.967	1	15.512 ± 0.066	10.288
2018 Aug 17 12:20	42.349	0.290	50.543	9.967	1	15.568 ± 0.029	10.344
2018 Aug 17 12:50	42.349	0.290	50.574	9.967	1	15.614 ± 0.029	10.390
2018 Aug 17 13:00	42.349	0.290	50.583	9.967	1	15.456 ± 0.056	10.232
2018 Aug 17 14:00	42.349	0.290	50.644	9.967	1	15.567 ± 0.059	10.343
2018 Aug 17 15:00	42.349	0.290	50.706	9.967	1	15.729 ± 0.073	10.505
2018 Aug 17 16:00	42.349	0.290	50.767	9.967	1	15.685 ± 0.062	10.461
2018 Aug 17 17:00	42.349	0.289	50.828	9.967	1	15.465 ± 0.056	10.248
2018 Aug 17 18:00	42.349	0.289	50.890	9.967	1	15.452 ± 0.055	10.235
2018 Aug 17 19:00	42.349	0.289	50.952	9.967	1	15.582 ± 0.059	10.365
2018 Aug 17 20:00	42.349	0.289	51.013	9.967	1	15.720 ± 0.062	10.503
2018 Aug 17 22:00	42.349	0.288	51.137	9.967	1	15.541 ± 0.058	10.332
2018 Aug 17 23:00	42.349	0.288	51.199	9.967	1	15.535 ± 0.059	10.326
2018 Aug 18 00:00	42.349	0.288	51.261	9.967	1	15.573 ± 0.059	10.364
2018 Aug 18 01:00	42.349	0.288	51.323	9.967	1	15.684 ± 0.061	10.475
2018 Sep 10 03:00	42.333	0.252	95.221	9.967	1	17.164 ± 0.103	12.246
2018 Sep 10 04:00	42.333	0.252	95.303	9.967	2	16.870 ± 0.091	11.952
2018 Sep 10 05:00	42.333	0.252	95.385	9.967	2	16.816 ± 0.110	11.898
2018 Sep 10 06:00	42.333	0.252	95.466	9.967	2	16.863 ± 0.091	11.945
2018 Sep 10 07:00	42.333	0.252	95.548	9.967	2	17.435 ± 0.128	12.517
2018 Sep 10 08:00	42.333	0.252	95.630	9.967	2	17.756 ± 0.162	12.838
2018 Sep 10 09:00	42.333	0.252	95.711	9.967	2	16.990 ± 0.089	12.072
2018 Sep 10 10:00	42.332	0.253	95.792	9.967	2	16.739 ± 0.078	11.812
2018 Sep 10 11:00	42.332	0.253	95.874	9.967	2	17.052 ± 0.095	12.125
2018 Sep 10 12:00	42.332	0.253	95.955	9.967	2	17.431 ± 0.124	12.504
2018 Sep 10 15:00	42.332	0.253	96.199	9.967	2	16.850 ± 0.088	11.923
2018 Sep 10 17:00	42.332	0.253	96.361	9.967	2	16.963 ± 0.090	12.036
2018 Sep 10 18:00	42.332	0.253	96.442	9.967	2	17.572 ± 0.141	12.645
2018 Sep 10 19:00	42.332	0.253	96.523	9.967	2	17.436 ± 0.219	12.509
2018 Sep 10 20:00	42.332	0.253	96.603	9.967	2	16.950 ± 0.095	12.023
2018 Sep 28 14:18	42.320	0.332	123.905	29.967	10	19.949 ± 0.489	14.433
2018 Sep 28 16:18	42.320	0.332	123.999	29.967	10	19.075 ± 0.193	13.559
2018 Sep 28 16:24	42.320	0.332	124.004	29.967	10	18.888 ± 0.169	13.372

Note.
[a] Color correction applied to transform LORRI magnitudes to Johnson V is +0.222 mag, using color from Benecchi et al. (2019) and the average color for scattered disk objects measured by Hainaut et al. (2012).

light curve with a total amplitude 0.9 mag. The observations taken at the highest phase angle $\alpha = 124°$ were too sparse to fit a separate light curve independently; however, folding the available data onto the light curve using the period fit at $\alpha = 51°$ (10.83012 hr) suggests that the light curve at $\alpha = 124°$ has an even higher amplitude.

Table 11
Earth-based Observations of CCKBO 2011 JY_{31}

Observation Mid-time	r (au)	Δ (au)	α (°)	Instrument	Filter	Total Images	Magnitude	V Magnitude at 1 au
2012 Sep 18 18:00	42.710	42.500	1.320	WFC3/*HST*[a]	F606W	2	24.96 ± 0.03	8.67
2014 Jun 25 09:12	42.625	41.615	0.174	HSC[b]	*r*	2	23.839 ± 0.065	7.785
2016 Jun 5 11:30	42.534	41.643	0.653	HSC	*r*	3	23.707 ± 0.024	7.657
2016 Jun 30 09:33	42.530	41.519	0.113	HSC	*r*	2	23.750 ± 0.048	7.706
2017 Jul 20 10:31	42.482	41.498	0.326	HSC	*r2*	16	23.673 ± 0.028	7.633
2017 Jul 21 07:06	42.482	41.502	0.348	HSC	*r2*	16	23.694 ± 0.034	7.654

Notes.
[a] Benecchi et al. (2015).
[b] Hyper Suprime-Cam (Miyazaki et al. 2012) on the National Astronomical Observatory of Japan's Subaru Telescope at Maunakea Observatory, Hawaii.

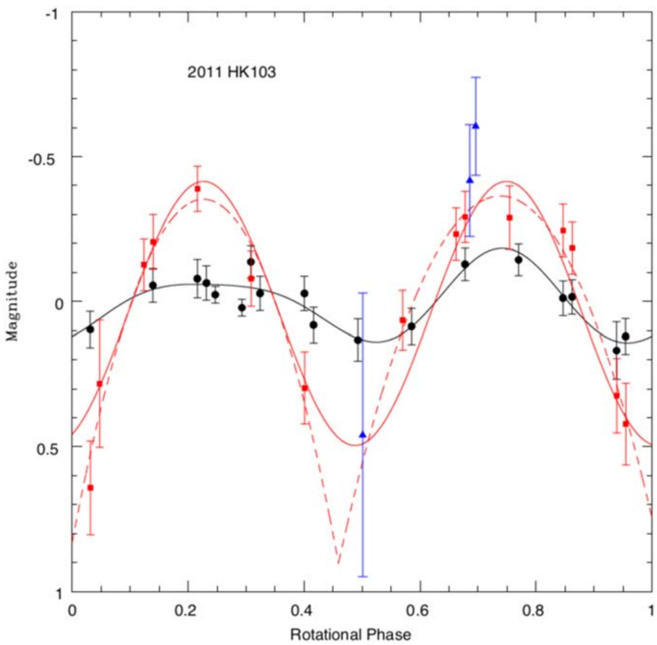

Figure 3. Rotation curve of scattered disk object HK_{103} from *New Horizons* LORRI observations acquired at three different epochs in 2017 August and September (Table 10). Solid black circles are data acquired at $\alpha = 51°$, red squares are data acquired at $\alpha = 96°$, and blue triangles are data acquired at $\alpha = 124°$. Black curve is a three-term Fourier fit to the $\alpha = 51°$ data with total amplitude 0.2 mag and a 10.83012 hr period. Data at $\alpha = 96°$ (red squares) and $\alpha = 124°$ (blue triangles) are scaled to the reflectance at $\alpha = 51°$ using the solar phase function of 2011 HK_{103} (Figure 5). Solid red line is a three-term Fourier fit to the $\alpha = 96°$ data with total amplitude 0.9 mag. Dashed red line is a fit to the $\alpha = 96°$ data with v-shaped minima, characteristic of contact binaries (Thirouin et al. 2010). Observations are phased to 2017 August 17 00:00.

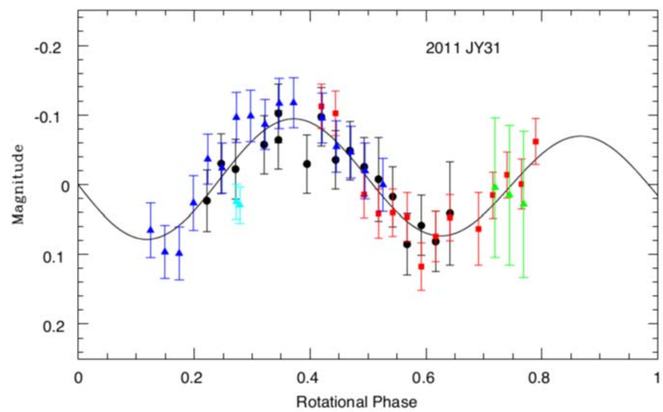

Figure 4. Rotation curve of CCKBO JY_{31} from *New Horizons* LORRI observations acquired at five different epochs in 2018 August and September (Table 12). Black circles are data acquired at $\alpha = 27°$, red squares are data acquired at $\alpha = 65°$, and blue triangles are data acquired at $\alpha = 85°$. Cyan and green triangles are data acquired at $\alpha = 58°$ and 122°, respectively. Black curve is a three-term Fourier fit to the data at $\alpha = 27°$, 65° and 85° with total amplitude 0.2 mag and a 40.52579 hr period. All observations are scaled to the reflectance at $\alpha = 27°$ using the solar phase function of 2011 JY_{31} (Figure 5). Observations are phased to 2018 August 19 00:00.

2.6. CCKBO 2011 JY_{31}

Table 11 summarizes Earth-based observations of the CCKBO 2011 JY_{31} (hereafter JY_{31}) acquired from Subaru and *HST* from 2012 to 2017 at phase angles between $\alpha = 0.^{\circ}11$ and $\alpha = 1.^{\circ}32$. *New Horizons* observed JY_{31} shortly after the spacecraft returned to three-axis mode in 2018 August (Table 12).

In contrast to HK_{103}, the rotational light curve of JY_{31} from the *New Horizons* LORRI data (Figure 4) does not increase in amplitude with increasing phase angle. A Lomb–Scargle periodogram analysis (Lomb 1976; Scargle 1982) of the observations acquired at $\alpha = 51°$ yields a statistically significant period of 40.52579 hr for JY_{31}. A three-term Fourier fit to the $\alpha = 27°$ data folded onto a rotation period of 40.52579 hr yields a double-peaked light curve with a total amplitude 0.2 mag. Folding the $\alpha = 65°$ and $\alpha = 85°$ data onto the same rotation period yields an identical double-peaked light curve that matches the $\alpha = 27°$ light curve. The consistency of the rotational light-curve amplitude of JY_{31} at three different phase angles suggests that this CCKBO may have a more uniform shape than HK_{103} and HE_{85}. However, the derivation of the shapes of these DKBOs based on the analysis of their rotational light curves is beyond the scope of this paper. See S. B. Porter et al. (2019, in preparation) for a detailed analysis of the rotational light curves and shapes of the six DKBOs presented herein. The observations taken at $\alpha = 58°$ and $\alpha = 122°$ were too sparse to fit separate light curves independently; however, folding these data onto the light curve using the 40.52579 hr period shows that they do not deviate significantly from the derived rotational light curve.

3. Solar Phase Curve Modeling

Combining Earth-based observations acquired at low phase angles ($\alpha < 1.^{\circ}5$) with those obtained by *New Horizons*

Table 12
LORRI Observations of CCKBO 2011 JY_{31}

Observation Mid-time	r (au)	Δ (au)	α (°)	Exposure Time (s)	Total Images	LORRI Magnitude	V Magnitude at 1 au[a]
2018 Aug 19 21:00	42.433	0.280	26.987	9.967	1	14.807 ± 0.044	9.664
2018 Aug 19 22:00	42.433	0.279	27.018	9.967	1	14.746 ± 0.043	9.610
2018 Aug 19 23:00	42.433	0.279	27.050	9.967	1	14.754 ± 0.043	9.618
2018 Aug 20 01:00	42.433	0.278	27.114	9.967	1	14.711 ± 0.042	9.583
2018 Aug 20 02:00	42.433	0.278	27.145	9.967	1	14.704 ± 0.042	9.576
2018 Aug 20 03:00	42.433	0.278	27.177	9.967	1	14.666 ± 0.042	9.538
2018 Aug 20 04:00	42.433	0.277	27.209	9.967	1	14.731 ± 0.042	9.611
2018 Aug 20 05:00	42.433	0.277	27.242	9.967	1	14.663 ± 0.042	9.543
2018 Aug 20 06:00	42.433	0.277	27.274	9.967	1	14.725 ± 0.042	9.605
2018 Aug 20 07:00	42.433	0.276	27.306	9.967	1	14.704 ± 0.042	9.592
2018 Aug 20 08:00	42.433	0.276	27.338	9.967	1	14.727 ± 0.042	9.615
2018 Aug 20 09:00	42.433	0.276	27.371	9.967	1	14.745 ± 0.060	9.633
2018 Aug 20 10:00	42.433	0.276	27.403	9.967	1	14.770 ± 0.043	9.658
2018 Aug 20 11:00	42.433	0.275	27.436	9.967	1	14.830 ± 0.044	9.726
2018 Aug 20 12:00	42.433	0.275	27.468	9.967	1	14.803 ± 0.043	9.699
2018 Aug 20 13:00	42.433	0.275	27.501	9.967	1	14.826 ± 0.043	9.723
2018 Aug 20 14:00	42.433	0.274	27.534	9.967	1	14.778 ± 0.074	9.682
2018 Sep 9 05:22	42.431	0.154	57.926	9.967	10	14.420 ± 0.025	10.575
2018 Sep 9 05:37	42.431	0.154	57.954	9.967	10	14.425 ± 0.026	10.580
2018 Sep 11 03:50	42.430	0.147	63.359	9.967	2	14.467 ± 0.032	10.723
2018 Sep 11 04:50	42.430	0.147	63.482	9.967	2	14.477 ± 0.032	10.733
2018 Sep 11 06:50	42.430	0.147	63.728	9.967	2	14.594 ± 0.033	10.850
2018 Sep 11 07:50	42.430	0.147	63.851	9.967	2	14.621 ± 0.035	10.877
2018 Sep 11 08:50	42.430	0.146	63.975	9.967	2	14.605 ± 0.034	10.876
2018 Sep 11 09:50	42.430	0.146	64.098	9.967	2	14.611 ± 0.035	10.882
2018 Sep 11 10:50	42.430	0.146	64.222	9.967	2	14.682 ± 0.034	10.953
2018 Sep 11 11:50	42.430	0.146	64.347	9.967	2	14.639 ± 0.036	10.910
2018 Sep 11 12:50	42.430	0.146	64.471	9.967	2	14.612 ± 0.033	10.883
2018 Sep 11 14:50	42.430	0.146	64.721	9.967	2	14.628 ± 0.052	10.899
2018 Sep 11 15:55	42.430	0.145	64.856	9.967	2	14.565 ± 0.033	10.851
2018 Sep 11 16:50	42.430	0.145	64.971	9.967	2	14.536 ± 0.033	10.822
2018 Sep 11 17:50	42.430	0.145	65.097	9.967	2	14.549 ± 0.036	10.835
2018 Sep 11 18:50	42.430	0.145	65.223	9.967	2	14.488 ± 0.033	10.774
2018 Sep 17 10:00	42.430	0.136	83.835	9.967	2	15.110 ± 0.039	11.535
2018 Sep 17 11:00	42.430	0.135	83.980	9.967	2	15.125 ± 0.038	11.566
2018 Sep 17 12:00	42.430	0.135	84.125	9.967	2	15.127 ± 0.038	11.568
2018 Sep 17 13:00	42.430	0.135	84.270	9.967	2	15.055 ± 0.039	11.496
2018 Sep 17 14:00	42.430	0.135	84.415	9.967	2	14.992 ± 0.036	11.433
2018 Sep 17 15:00	42.430	0.135	84.560	9.967	2	15.005 ± 0.036	11.446
2018 Sep 17 16:00	42.430	0.135	84.705	9.967	2	14.932 ± 0.036	11.373
2018 Sep 17 17:00	42.430	0.135	84.850	9.967	2	14.930 ± 0.037	11.371
2018 Sep 17 18:00	42.430	0.135	84.995	9.967	2	14.942 ± 0.036	11.383
2018 Sep 17 19:00	42.430	0.135	85.140	9.967	2	14.912 ± 0.036	11.353
2018 Sep 17 20:00	42.430	0.135	85.286	9.967	2	14.911 ± 0.036	11.352
2018 Sep 17 22:00	42.430	0.135	85.576	9.967	2	14.933 ± 0.036	11.374
2018 Sep 17 23:00	42.430	0.135	85.721	9.967	2	14.974 ± 0.037	11.415
2018 Sep 18 00:00	42.430	0.135	85.866	9.967	2	14.982 ± 0.037	11.423
2018 Sep 18 01:00	42.430	0.135	86.011	9.967	2	15.009 ± 0.040	11.450
2018 Sep 18 02:00	42.430	0.135	86.193	9.967	2	15.029 ± 0.038	11.470
2018 Sep 30 05:47	42.428	0.170	122.268	29.967	7	17.948 ± 0.100	13.888
2018 Sep 30 06:47	42.428	0.170	122.359	29.967	7	17.959 ± 0.100	13.899
2018 Sep 30 07:47	42.428	0.170	122.450	29.967	7	17.972 ± 0.105	13.912

Note.
[a] Color correction applied to transform LORRI magnitudes to Johnson V is +0.441 mag, using color from Benecchi et al. (2015) and the average color for CCKBOs measured by Hainaut et al. (2012).

LORRI at higher phase angles ($19° < \alpha < 131°$) enables the production of disk-integrated solar phase curves for each DKBO. Figure 5 shows the complete solar phase curves for all six DKBOs, and Figure 6 highlights the near-opposition portions at $\alpha < 1\overset{\circ}{.}5$ from Earth-based observations. Only the Earth-based observations of Arawn and JY_{31} have been corrected for rotational variation in reflectance (i.e., light curve). For the remaining DKBOs, we average all observations

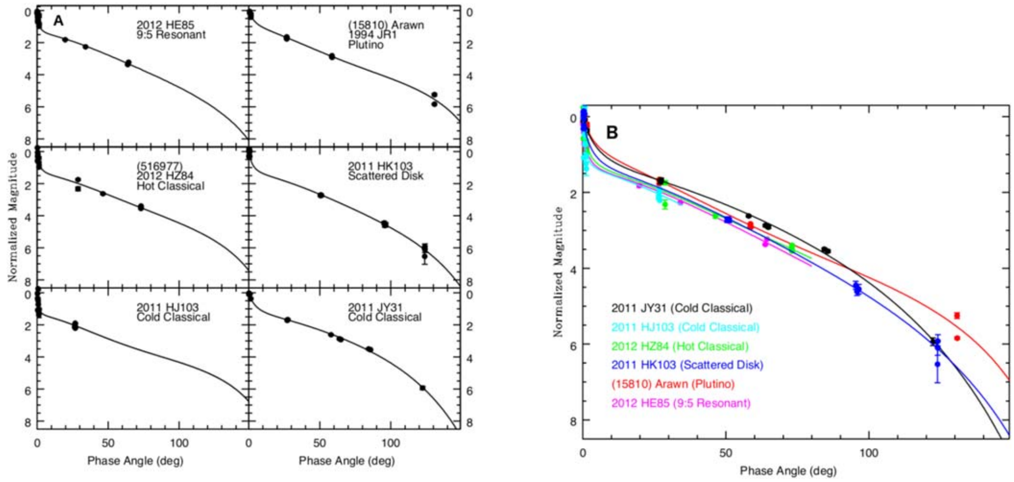

Figure 5. Complete solar phase curves of all six distant KBOs in this study plotted separately (A) and together (B) to facilitate direct comparison of their shapes. All phase curves are normalized to 0 mag at opposition ($\alpha = 0°$) and shown on the same scale. Arawn's phase curve includes two observations at $\alpha = 131°$, which were not included in the Porter et al. (2016) study. Solid lines are fits to the Hapke (2012) photometric model described for each DKBO by the parameters in Table 13; however, the solid lines in (B) for HJ_{103}, HE_{85}, and HZ_{84} are limited to phase angles no larger than 30°, 80°, and 80°, respectively, because there are no observations of these DKBOs at higher phase angles. Limiting the range of phase angles for these DKBOs enables comparisons between the shapes of Arawn, HK_{103}, and JY_{31} which do have observations at higher phase angles. Only some of the *New Horizons* LORRI observations have been corrected for variation in reflectance with rotation (i.e., light curve). (See the text for details.)

on a given night (Tables 3, 5, 7, and 9) and otherwise make no corrections for light-curve or rotational variation in reflectance. For DKBOs with many observations obtained at a regular cadence during a night and rotation periods less than 8 hr, averaging all nightly observations may approximate the light-curve-corrected reflectance at a given phase angle. Clearly, HJ_{103} has a high-amplitude light curve that must be removed to characterize the opposition effect for this CCKBO, but insufficient sampling of Earth-based observations (Table 7) precludes construction of HJ_{103}'s light curve at low phase angles. Because we use data from multiple filters and photometric systems, color corrections must transform all observations to a single wavelength, here the *V*-magnitude (VEGAMAG) system (Tables 1–12). For the DKBOs with available light curves from *New Horizons* LORRI, i.e., Arawn, HE_{85}, HK_{103}, and JY_{31}, we adopt the light-curve mean as the reflectance at each phase angle.

Upon construction of the complete solar phase curves, we normalize all observations to the geometric albedo at opposition and fit them to the Hapke (2012) photometric model modified following Helfenstein & Shepard (2011). Since we do not know the diameters of these DKBO targets, we must assume that their geometric albedos match those of the average objects in their dynamical classes reported by Lacerda et al. (2014; Table 14).

3.1. Hapke Parameters

Eight parameters describe the Hapke (2012) model: single scattering albedo, surface macroscopic roughness, two parameters that describe the single particle phase function (SPPF), and four parameters that describe the opposition effect, the dramatic, nonlinear increase in reflectance seen as phase angles decrease to zero. The Hapke (2012) model also includes a porosity coefficient, *K*; however, our approach uses the Helfenstein & Shepard (2011) version which eliminates the need for the *K* parameter. We describe each parameter in detail below, for more detailed descriptions, see reviews by Verbiscer & Helfenstein (1998) and Verbiscer et al. (2013).

By definition, the single scattering albedo $\tilde{\omega}_o$ is the ratio of particle scattering to extinction efficiencies; it is related to particle composition, size, and microstructure. The macroscopic roughness parameter $\bar{\theta}$ is the mean topographic slope angle of surface relief at resolutions below the pixel scale of the observations. The opposition effect is the product of two phenomena: particle shadow hiding and a constructive interference phenomenon known as coherent backscatter (Shkuratov 1988; Muinonen 1990). Both the shadow hiding opposition effect (SHOE) and the coherent backscatter opposition effect (CBOE) are described by two parameters, an amplitude B_o and an angular width h expressed in radians. The angular width of the SHOE h_S is related to the porosity and particle size distribution of surface particles. The amplitude of the SHOE B_{oS} is related to particle transparency; it is the fraction of light backscattered directly from the front surface of a particle relative to the total amount of light backscattered by the particle. For a perfectly opaque particle, $B_{oS} = 1$. The angular width h_C and amplitude B_{oC} of the CBOE depend on the density and size of small scatterers and the mean optical path length of a photon (medium transparency). Both B_{oS} and B_{oC} have upper limits of unity.

We use a two-parameter Henyey & Greenstein (1941) SPPF which is a linear combination of two single-parameter Henyey–Greenstein functions (McGuire & Hapke 1995):

$$P(\alpha, b, c) = \frac{(1+c)}{2}\frac{(1-b^2)}{(1-2b\cos(\alpha)+b^2)^{3/2}} + \frac{(1-c)}{2}\frac{(1-b^2)}{(1+2b\cos(\alpha)+b^2)^{3/2}}. \quad (2)$$

The *b* parameter describes the (assumed to be equal) angular width of the backward and forward scattering lobes of the particle phase function and the *c* parameter describes the relative amplitude of each lobe. The two parameters characterize the mechanical structure of surface grains: surfaces with

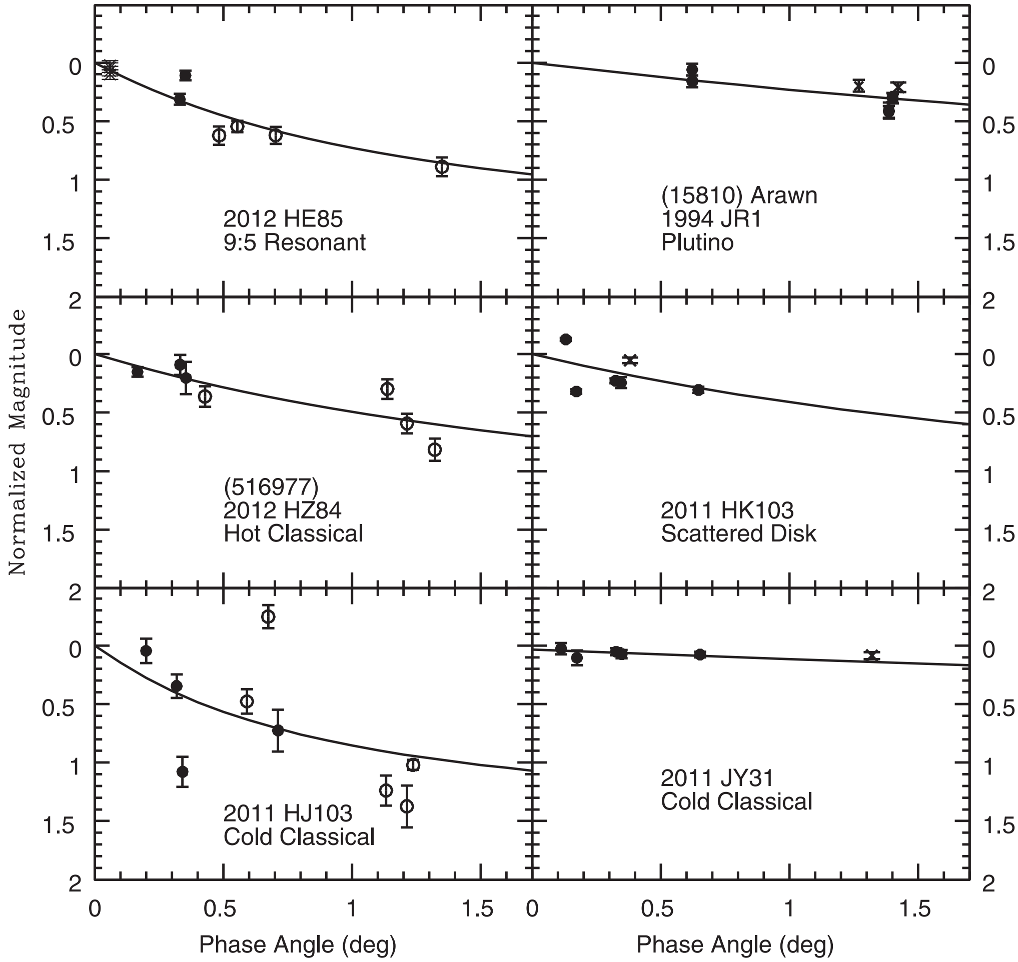

Figure 6. Near-opposition portions of all solar phase curves in Figure 5 from the Earth-based observations in Tables 1, 3, 5, 7, 9, and 11 for each DKBO. Solid circles represent observations from the Hyper Suprime-Cam on Subaru, open circles are observations from Megacam at Magellan, and open triangles are observations from *HST*. The scatter in these low phase angle points is due to the variation in reflectance with rotation (i.e., light curve); however, only the Arawn observations have been corrected for light curve.

Table 13
Hapke (2012) Parameters for the DKBOs in This Study

Distant KBO	Class	$\tilde{\omega}_o$	$\bar{\theta}$	SPPF b	SPPF c	SHOE Width	SHOE Amplitude	CBOE Width	CBOE Amplitude	χ^2 Residual
(15810) Arawn	3:2	0.08	28	0.41	−0.04	0.045	0.78	0.058	0.85	0.0121
2011 HJ_{103}	CC	0.14	27	0.45	−0.27	0.0058	1.00	0.012	1.00	0.204
2011 JY_{31}	CC	0.14	25	0.23	1.47	0.22	1.00	0.13	1.00	0.0053
(516977) 2012 HZ_{84}	HC	0.06	26	0.37	0.21	0.013	1.00	0.021	1.00	0.067
2011 HK_{103}	SD	0.035	23	0.34	0.89	0.015	1.00	0.048	1.00	0.0623
2012 HE_{85}	9:5	0.10	30	0.37	0.44	0.0088	1.00	0.016	1.00	0.0223

$b < 0.5$ have irregularly shaped, rougher particles and surfaces with $b > 0.5$ have euhedral, smoother particles. Similarly, particles with $c < 0$ have a lower density of internal scatterers and are thus more transparent, while particles with $c > 0$ have higher densities of internal scatterers and are more opaque.

4. Results

Table 13 summarizes the sets of Hapke parameters derived from fits to the solar phase curves for each DKBO. The solid lines in Figures 5 and 6 are the model disk-integrated solar phase curves for each DKBO Hapke fit. Each phase curve in Figures 5 and 6 is normalized to magnitude zero at opposition to facilitate comparison between the phase functions of all six DKBOs.

4.1. Single Scattering Albedos and Macroscopic Roughness Parameters

Since we had to assume geometric albedos from Lacerda et al. (2014), our derived single scattering albedos are directly related to this assumed geometric albedo. Until diameters are determined for these DKBOs, either by stellar occultation or thermal radiometric measurements, the geometric albedos, single scattering albedos, and Bond albedos can only be estimated using these average values. The mean topographic

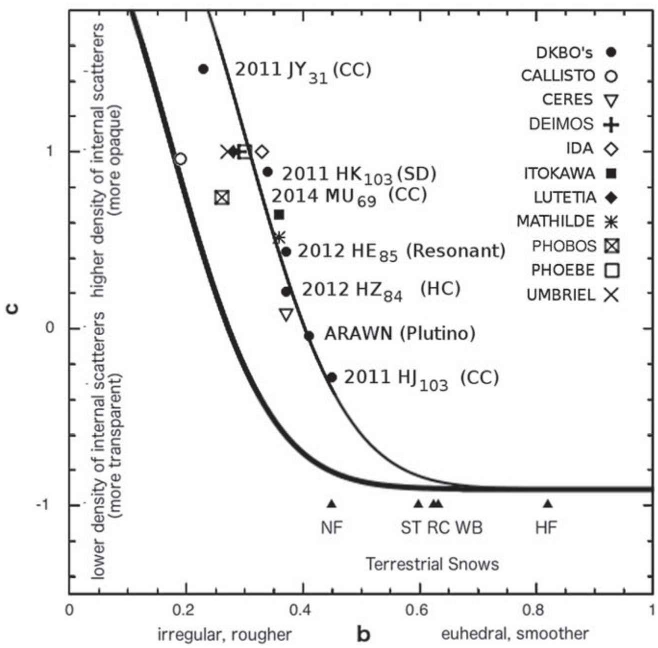

Figure 7. McGuire–Hapke (McGuire & Hapke 1995) SPPF c vs. b parameter (hockey stick) plot including parameters for all KBOs observed by *New Horizons* (solid circles) and those for a wide variety of other dark solar system bodies. Note that for HJ_{103} b and c are not well constrained since there are no data for that CCKBO at $\alpha > 27°$. Data points for other dark outer solar system bodies have been transformed from their published SPPF form parameters to the McGuire–Hapke b, c system using conversion relations adapted from Verbiscer et al. (2018a) and given in Table 15. Data points are shown for Callisto (Buratti 1991; Domingue & Verbiscer 1997), Ceres (Li et al. 2019), Deimos (Thomas et al. 1996), Ida (Helfenstein et al. 1996), Itokawa (Tatsumi et al. 2018), Lutetia (Masoumzadeh & Boehnhardt 2019), Mathilde (Clark et al. 1999), MU_{69} (Stern et al. 2019), Phobos (Simonelli et al. 1998), Phoebe (Simonelli et al. 1999; Miller et al. 2011), and Umbriel (Helfenstein et al. 1989; Buratti & Mosher 1991). Also shown for comparison are parameters for terrestrial snow and frost surfaces (solid triangles; Verbiscer & Veverka 1990; Domingue et al. 1997) including new-fallen snow (NF), settling snow (ST), rain crust (RC), wind-blown snow (WB), and hoarfrost (HF). The thick, solid curve represents Hapke's empirical hockey stick relation (Hapke 2012), $c = 3.29\exp(-17.4b^2) - 0.908$, that approximates the behavior of a broad range of particulate surfaces and may represent most particles found in regoliths. The surfaces of the CCKBOs and scattered disk (SD) objects are more backscattering than those of the hot classical (HC) and resonant objects (9:5 and 3:2, plutino). This more strongly backscattering behavior parallels the hockey stick curve as shown as a thin curve, but the trend is shifted toward characteristics of smoother, more euhedral particle shapes b valuesby 0.13 ± 0.01. The plot shows that this trend is characteristic of many low-albedo solar system bodies.

slope angles, or roughness, are all very similar, ranging from 23° to 30°.

4.2. Phase Integrals, Phase Coefficients, and Bond Albedos

Table 14 lists the geometric albedos, phase coefficients, phase integrals, and Bond albedos for each DKBO. Phase coefficients β (phase curve slopes) are measured between phase angles 10° and 50°, in the linear portion of the phase curves. Despite the diversity in dynamical classes, the phase coefficients are remarkably similar for all six DKBOs, as Figure 5(B) illustrates, ranging between 0.0291 and 0.0362 mag/deg. Beyond $\alpha = 80°$, however, the shapes of the phase curves of Arawn, JY_{31}, and HK_{103} differ from one another, although insufficient sampling of their light curves at the highest phase angles limits the robustness of this conclusion. (Of course the limited range of phase angles for HJ_{103} means that the photometric and Hapke parameters constrained by observations at phase angles $\alpha > 20°$ deg are not at all well constrained.) We calculate the phase integral q using the approximation provided by Verbiscer & Veverka (1988),

$$q = 0.135 + 2.671\Phi(70), \tag{3}$$

where $\Phi(70)$ is the normalized albedo at $\alpha = 70°$.

4.3. Opposition Effect Parameters

Without corrections to the rotational phase curve at low phase angles, the opposition effect amplitudes and angular widths are not well constrained for objects that have high-amplitude light curves such as HJ_{103}. All opposition effect amplitudes are equal to unity, with the exception of Arawn.

4.4. Single Particle Phase Functions (SPPFs)

Aside from the single scattering albedos, the SPPF parameters b and c are the only parameters where differences are apparent among the DKBO dynamical classes. Plots of b versus c for particles of different transparencies and shapes occupy a parameter space that is restricted to values yielding a shape resembling a hockey stick (Hapke 2012). Figure 7 shows such a hockey stick plot for the six DKBOs and other dark, airless solar system objects. The thick, solid curve is Hapke's (Hapke 2012) empirical hockey stick relation, which approximates the behavior of a broad range of particulate surfaces. It may be considered a first-order model of most of the particles found in planetary regoliths. The *New Horizons* DKBO results define a trend (thin line in Figure 7) which parallels the thick hockey stick curve, but the trend is shifted toward characteristics of smoother, more euhedral particle shapes, b values, by -0.13 ± 0.01. Published results for a wide variety of other dark, airless solar system bodies also follow this trend. Callisto falls directly on the hockey stick curve and thus deviates from the SPPF of other dark, airless bodies shown in Figure 7. Phoebe lies about halfway between the two curves. For Phoebe, it is worth noting that the plotted point is an average of two solutions (see Table 15) that were obtained under different assumptions about the SHOE amplitude B_{os}. In Solution 1, the SHOE amplitude was allowed to vary to an unrealistically large value ($B_{oS} = 3.4$) in comparison to its physical limit of unity, and the corresponding SPPF parameters are $b = 0.24^{+0.26}_{-0.11}$ and $c = 1$. Phoebe would plot closer to Callisto on the hockey stick curve (although with very large uncertainties). For Solution 2, the value of the SHOE amplitude was fixed at a value ($B_{oS} = 2.0$) that is closer to the physical limit. The corresponding 2PHG values ($b = 0.36 \pm 0.03$, $c = 1$) would place it just to the right of the dark body trend, but still within the expected uncertainty. Both of these solutions were obtained prior to the incorporation of the CBOE into Hapke's model. More recent work that includes both CBOE and SHOE in the Hapke model (Miller et al. 2011) restricts the SHOE amplitude to its physical limit $B_{oS} = 1.0$ and agrees best with Solution 2.

The DKBO dark body trend, like the hockey stick trend, exhibits a weak correlation of increasing c with decreasing b. One interpretation of this trend is that characterizes how the microstructure of superficially similar regolith grains evolve with time and exposure to the space environment. It suggests that as the dark particles evolve to rougher, more irregular shapes, they simultaneously tend to develop an increasing density of internal scatterers. The SPPF angular widths b span a

Table 14
Geometric Albedo, Phase Coefficient, Phase Integral, and Bond Albedo for the DKBOs in This Study

DKBO	Class	Phase Angle Range (°)	Geometric Albedo p_V[a]	Geometric Albedo p_V[b]	Phase Coefficient β (mag/deg)[c]	Phase Integral q[d]	Bond Albedo A_B[e]
(15810) Arawn	3:2	0.3–131	$0.09^{+0.07}_{-0.04}$	0.081	0.0362	0.262	0.0212
2011 HJ_{103}	CC	0.2–27	$0.15^{+0.08}_{-0.06}$	0.149	0.0332	0.241	0.0360
2011 JY_{31}	CC	0.1–122	$0.15^{+0.08}_{-0.06}$	0.147	0.0291	0.302	0.0446
(516977) 2012 HZ_{84}	HC	0.1–73	$0.08^{+0.05}_{-0.04}$	0.073	0.0301	0.252	0.0184
2011 HK_{103}	SD	0.1–124	$0.05^{+0.04}_{-0.01}$	0.055	0.0325	0.248	0.0136
2012 HE_{85}	9:5	0.06–64	$0.13^{+0.09}_{-0.05}$	0.138	0.0317	0.237	0.0326

Notes.
[a] Median geometric albedos and their uncertainties for each DKBO dynamical class (Lacerda et al. 2014).
[b] Geometric albedos derived from the Hapke (2012) model fits (Table 13) to the data after normalizing to the p_V from Lacerda et al. (2014).
[c] Phase coefficients β measured between phase angles $\alpha = 10°$ and $50°$.
[d] Phase integrals q calculated using the approximation $q = 0.135 + 2.671\Phi(70)$, where $\Phi(70)$ is the normalized albedo at $\alpha = 70°$ (Verbiscer & Veverka 1988).
[e] Bond albedo $A_B = pq$ calculated using assumed geometric albedos from Lacerda et al. (2014).

Table 15
Conversions from Published SPPF Parameters to McGuire–Hapke b, c Values

Object	Source	SPPF Type	SPPF Parameters	Conversion Relations	(b, c) Values
Phobos	Simonelli et al. (1998)	3PHG	$g_1 = -0.20 \pm 0.04$	$b = (1-f)\lvert g_1\rvert + f\lvert g_2\rvert$	$b = 0.26 \pm 0.05$
			$g_2 = 0.66 \pm 0.01$	$c = 1\text{–}2f$	$c = 0.74 \pm 0.05$
			$f = 0.13 \pm 0.09$		
Deimos	Thomas et al. (1996)	1PHG	$g_1 = -0.29 \pm 0.03$	$b = \lvert g_1\rvert$	$b = 0.29 \pm 0.03$
				$c = 1$	$c = 1$
21 Lutetia	Masoumzadeh & Boehnhardt (2019)	1PHG	$g_1 = -0.28 \pm 0.01$	$b = \lvert g_1\rvert$	$b = 0.28 \pm 0.01$
				$c = 1$	$c = 1$
243 Ida	Helfenstein et al. (1996)	1PHG	$g_1 = -0.33 \pm 0.01$	$b = \lvert g_1\rvert$	$b = 0.33 \pm 0.01$
				$c = 1$	$c = 1$
253 Mathilde	Clark et al. (1999)	3PHG	$g_1 = -0.27 \pm 0.04$	$b = (1-f)\lvert g_1\rvert + f\lvert g_2\rvert$	$b = 0.36 \pm 0.05$
			$g_2 = 0.66 \pm 0.01$	$c = 1\text{–}2f$	$c = 0.52 \pm 0.05$
			$f = 0.24 \pm 0.09$		
Callisto	Domingue & Verbiscer (1997)	Domingue	$b' = 0.17 \pm 0.01$	$b = b'$	$b = 0.17 \pm 0.01$
		2PHG	$c' = 0.95 \pm 0.01$	$c = 2c' - 1$	$c = 0.91 \pm 0.02$
	Buratti (1991)	1PHG	$g_1 = -0.20 \pm 0.03$	$b = \lvert g_1\rvert$	$b = 0.20 \pm 0.3$
				$c = 1$	$c = 1$
Phoebe	Simonelli et al. (1999)	1PHG	$g_1 = -0.24^{+0.26}_{-0.11}$	$b = \lvert g_1\rvert$	$b = 0.24^{+0.26}_{-0.11}$
	(Solution #1)			$c = 1$	$c = 1$
	Simonelli et al. (1999)	1PHG	$g_1 = -0.36 \pm 0.03$	$b = \lvert g_1\rvert$	$b = 0.36 \pm 0.03$
	(Solution #2)			$c = 1$	$c = 1$
Umbriel	Helfenstein et al. (1988)	1PHG	$g_1 = -0.28 \pm 0.01$	$b = \lvert g_1\rvert$	$b = 0.28 \pm 0.01$
				$c = 1$	$c = 1$
	Buratti & Mosher (1991)	1PHG	$g_1 = -0.25 \pm 0.01$	$b = \lvert g_1\rvert$	$b = 0.25 \pm 0.01$
				$c = 1$	$c = 1$

relatively narrow range from 0.23 to 0.49, indicating that particle structures on these DKBO surfaces do not differ significantly. Particles on the surface of the cold classical JY_{31} ($b = 0.23$) are more irregularly shaped and rougher than those on the surface of Arawn ($b = 0.49$). The SPPF amplitudes c, however, span a broader range from −0.45 to 1.47, indicating that particles on these DKBOs vary in their relative opacities. Particles on the surface of JY_{31} are more opaque ($c = 1.47$) than those on Arawn ($c = -0.04$); however, Arawn's $\alpha = 131°$ data are sparse and not fully corrected for light-curve variations. Arawn's light curve at smaller phase angles also has a higher amplitude than JY_{31}'s; therefore, the more forward scattering SPPF derived for Arawn may be due to anomalously high reflectances at high phase angles since *New Horizons* did not measure Arawn's complete light curve at $\alpha = 131°$.

Caution must be taken, however, when interpreting SPPFs derived from disk-integrated phase curves of nonspherical objects. Given the variation in their light-curve amplitudes at different phase angles, it is highly likely that these DKBOs, with the exception of JY_{31}, are nonspherical. The low (0.2 mag) amplitude of JY_{31}'s light curve, coupled with the fact that the amplitude does not increase with increasing phase angle, strongly suggests that JY_{31} is spherical. Additionally, the

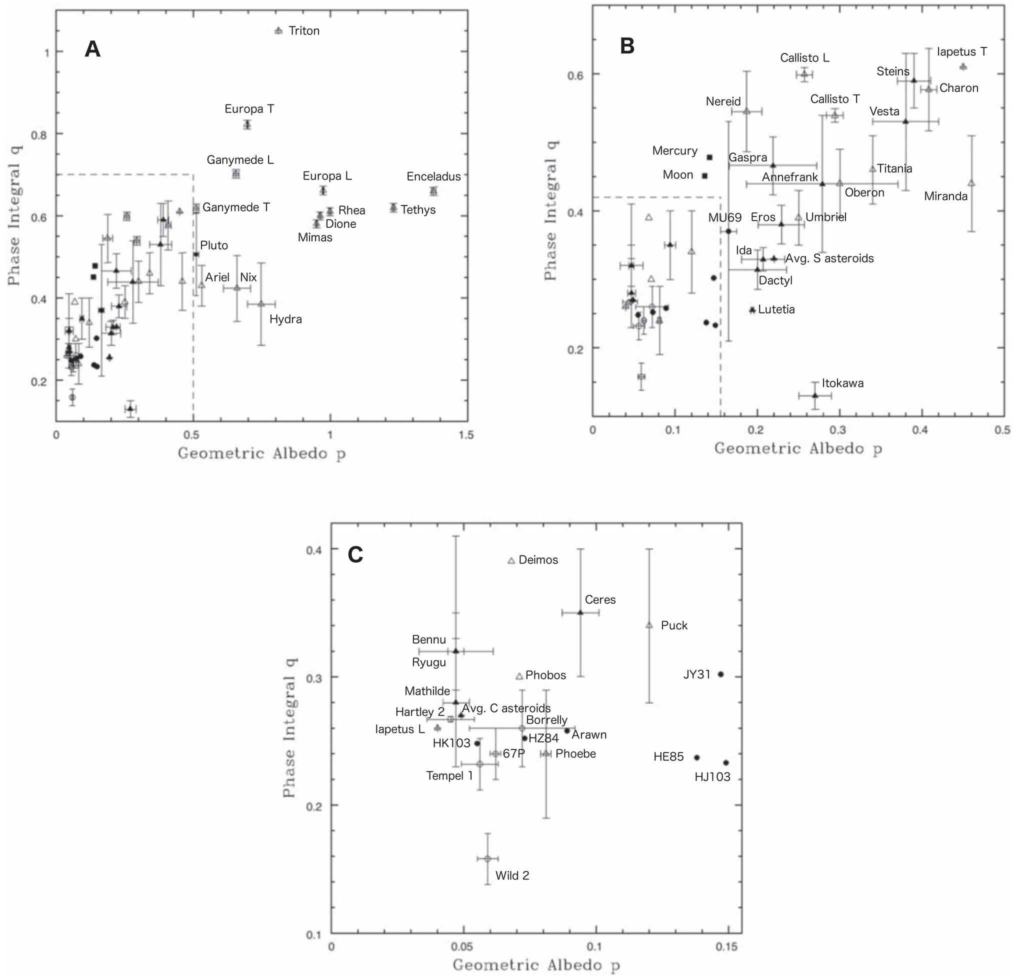

Figure 8. Phase integral q vs. visible geometric albedo p_V for all objects in the solar system that have been observed at phase angles large enough to evaluate their phase integrals. Solid circles are KBOs, open circles are comets, open triangles are satellites, and solid triangles are asteroids. L and T denote leading and trailing hemispheres, respectively. Solid squares represent the Moon and Mercury. Generally, observations at $\alpha > 70°$ are required to estimate phase integrals (Verbiscer & Veverka 1988). Panel (A) contains all objects, however, to facilitate the identification and location of objects with $p_v < 0.5$, panel (B) corresponds to the area within the box defined by the dashed lines in panel (A); panel (C) corresponds to the area within the box defined by the dashed lines in panel (B; i.e., those objects with $p_V < 0.15$ and $q < 0.4$). Data points are shown for Triton (Hillier et al. 1990); Nereid (Thomas et al. 1991),; Europa, Ganymede, Callisto (Domingue & Verbiscer 1997); Mimas, Enceladus, Tethys, Dione, Rhea (Verbiscer et al. 2007); Iapetus (Blackburn et al. 2010); Phoebe (Simonelli et al. 1999; Miller et al. 2011); Phobos (Simonelli et al. 1998); Deimos (Thomas et al. 1996); Miranda, Ariel, Umbriel, Titania, Oberon, Puck (Karkoschka 2001); Pluto, Charon (Verbiscer et al. 2019); Nix, Hydra (Verbiscer et al. 2018b); Mercury (Warell & Bergfors 2008); Moon (Helfenstein & Veverka 1987); Ceres (Ciarniello et al. 2017); Vesta (Li et al. 2013); Eros (Li et al. 2004); Ida, Dactyl, Gaspra (Helfenstein et al. 1996); Mathilde (Clark et al. 1999); Lutetia (Masoumzadeh et al. 2015); Steins (Spjuth et al. 2012); Annefrank (Hillier et al. 2011); Itokawa (Tatsumi et al. 2018); Bennu (Takir et al. 2015); Ryugu (Ishiguro et al. 2014); C and S asteroids (Helfenstein & Veverka 1989); Borrelly (*R*-band), Hartley 2, Tempel 1, Wild 2 (Li et al. 2013); 67P (Ciarniello et al. 2015); and MU69 (Stern et al. 2019).

consistent, low amplitude of JY_{31}'s light curve viewed at a variety of phase angles indicates likely sphericity because the amplitude would change with phase angle if JY_{31}'s rotation axis were aligned with the LORRI boresight in any one epoch. Li et al. (2004, 2003) have shown that assuming a spherical shape for asteroids such as Eros, may introduce significant errors, especially at high phase angles, resulting in more forward scattering phase functions than actually exhibited. Hillier et al. (2011) also found this effect to be true in their analysis of main belt asteroid (5535) Annefrank by the *Stardust* spacecraft.

5. Discussion

To enable comparisons between the surface scattering properties of these DKBOs observed by *New Horizons* with those of MU_{69} and other solar system objects, we examine the phase integral q as a function of the visible geometric albedo p_V (Figure 8). Again, the geometric albedos for the DKBOs in this study are assumed from the values reported by Lacerda et al. (2014) for each dynamical class, so their placement along the horizontal axis in Figure 8 is only approximate. The DKBO phase integrals, however, are insensitive to p_V, since the phase integral is measured from a normalized solar phase curve; therefore, the locations of these DKBOs on the vertical axis correspond to the phase integrals determined for each DKBO (Table 14), not approximations based on dynamical class.

Brucker et al. (2009) proposed a linear relationship between the phase integral and geometric albedo using preliminary values for several solar system objects, however, using updated values for both q and p_V (Figure 8) demonstrates that the relationship between the two quantities is not linear for all geometric albedos. Large objects (>400 km in diameter) tend to have higher geometric albedos and phase integrals; their phase curves are shallower than those of smaller, darker bodies. Small bodies, especially comet nuclei and small asteroids, have the lowest phase integrals and albedos (Figure 8(C)). Most comet nuclei have p_V between 0.03 and 0.07 and phase integrals q between 0.22 and 0.3, with the exception of comet 81P/Wild 2 which has an exceptionally low phase integral ($q = 0.16$; Li et al. 2013), owing to its steep phase curve. With the exception of the cold classical JY_{31}, the DKBOs in this study have phase integrals of $q \sim 0.25$, meaning that the shapes of their solar phase curves are commensurate with those of other small bodies in the solar system, particularly the nuclei of JFCs. The phase integral and albedo of Saturn's irregular satellite Phoebe, thought to be a captured KBO (Johnson & Lunine 2005), are similar to those of these DKBOs. The phase integral of the cold classical JY_{31}, $q = 0.3$, is higher than the other DKBOs in this study, yet it comes closest to that of MU_{69}, $q = 0.37 \pm 0.16$ (Stern et al. 2019). The other cold classical DKBO, HJ_{103}, has no observations at phase angles larger than $\alpha = 27°$, so its phase curve shape and phase integral are not well constrained. Therefore, although the sample is small, it appears that the cold classicals share scattering properties, while the rest of the DKBOs studied here (hot classicals, resonant, and scattered disk objects) are similar to each other and distinct from the cold classicals.

6. Summary

From 2015 November through 2018 September, *New Horizons* LORRI observed six long-range KBOs at solar phase angles ranging from $\alpha = 19°$ to 131°. These DKBOs included two cold classicals (2011 JY_{31} and 2011 HJ_{103}), one hot classical (516977) 2012 HZ_{84}, one plutino (15810) Arawn (1994 JR_1), one resonant (2012 HE_{85}), and one object from the scattered disk (2011 HK_{103}). The observations of CCKBOs 2011 HJ_{103} and 2011 JY_{31} provide context for *New Horizons'* 2019 January 1 close flyby of CCKBO 2014 MU_{69} and suggest that cold classicals share scattering properties that are similar to each other, but distinct from the other KBO dynamical classes, albeit with a small sample size. The microphysical structure of regolith grains implied by the particle phase functions of these DKBOs vary both in grain shape and the density of internal scatterers. These variations follow a uniform trend from rough, irregularly shaped grains with low opacity to smoother shaped grains that are more transparent—a trend that is shared with many other low-albedo airless solar system bodies.

Work supported by the New Horizons project. Based on observations made with the NASA/ESA *Hubble Space Telescope*, obtained from the data archive at the Space Telescope Science Institute. STScI is operated by the Association of Universities for Research in Astronomy, Inc. under NASA contract NAS 5-26555. These observations are associated with programs 9060, 12535, and 14092. P.H. gratefully acknowledges support from NASA Planetary Geology and Geophysics Program grant NNX14AN04G.

Facilities: HST (WFPC2, WFC3), *New Horizons* (LORRI), Subaru (HSC), Magellan (Megacam).

ORCID iDs

Anne J. Verbiscer https://orcid.org/0000-0002-3323-9304
Simon Porter https://orcid.org/0000-0003-0333-6055
Susan D. Benecchi https://orcid.org/0000-0001-8821-5927
J. J. Kavelaars https://orcid.org/0000-0001-7032-5255
Harold A. Weaver https://orcid.org/0000-0003-0951-7762
Marc W. Buie https://orcid.org/0000-0003-0854-745X
David Tholen https://orcid.org/0000-0003-0773-1888
Alex H. Parker https://orcid.org/0000-0002-6722-0994
Catherine B. Olkin https://orcid.org/0000-0002-5846-716X
Kelsi N. Singer https://orcid.org/0000-0003-3045-8445
Carey M. Lisse https://orcid.org/0000-0002-9548-1526

References

Benecchi, S. D., Borncamp, D., Parker, A. H., et al. 2019, Icarus, in press
Benecchi, S. D., Noll, K. S., Stephens, D. C., Grundy, W. M., & Rawlins, J. 2011, Icar, 213, 693
Benecchi, S. D., Noll, K. S., Weaver, H. A., et al. 2015, Icar, 246, 369
Blackburn, D. G., Buratti, B. J., Ulrich, R., & Mosher, J. A. 2010, Icar, 209, 738
Brucker, M. J., Grundy, W. M., Stansberry, J. A., et al. 2009, Icar, 201, 284
Buie, M. W., Porter, S. B., Tamblyn, P., et al. 2019, ApJ, submitted
Buratti, B. J. 1991, Icar, 92, 312
Buratti, B. J., & Mosher, J. A. 1991, Icar, 90, 1
Cheng, A. F., Weaver, H. A., Conard, S. J., et al. 2008, SSRv, 140, 189
Ciarniello, M., Capaccioni, F., Filacchione, G., et al. 2015, A&A, 583, A31
Ciarniello, M., De Sanctis, M. C., Ammannito, E., et al. 2017, A&A, 598, A130
Clark, B. E., Veverka, J., Helfenstein, P., et al. 1999, Icar, 140, 53
Denk, T., & Mottola, S. 2019, Icar, 322, 80
Domingue, D., Hartman, B., & Verbiscer, A. 1997, Icar, 128, 28
Domingue, D., & Verbiscer, A. 1997, Icar, 128, 49
Gaia Collaboration, Brown, A. G. A., Vallenari, A., et al. 2018, A&A, 616, A1
Green, S. F., McBride, N., O'Ceallaigh, D. P., et al. 1997, MNRAS, 290, 186
Hainaut, O. R., Boehnhardt, H., & Protopapa, S. 2012, A&A, 546, A115
Hapke, B. 2012, Icar, 221, 1079
Helfenstein, P., & Shepard, M. K. 2011, Icar, 215, 83
Helfenstein, P., Thomas, P. C., & Veverka, J. 1989, Natur, 338, 324
Helfenstein, P., Veverka, J., & Thomas, P. C. 1988, Icar, 74, 231
Helfenstein, P., & Veverka, J. 1987, Icar, 72, 342
Helfenstein, P., & Veverka, J. 1989, in Asteroids II, ed. R. P. Binzel, T. Gehrels, & M. S. Matthews (Tucson, AZ: Univ. Arizona Press), 557
Helfenstein, P., Veverka, J., Thomas, P. C., et al. 1996, Icar, 120, 48
Henyey, L. G., & Greenstein, J. L. 1941, ApJ, 93, 70
Hillier, J., Helfenstein, P., Verbiscer, A., et al. 1990, Sci, 250, 419
Hillier, J. K., Bauer, J. M., & Buratti, B. J. 2011, Icar, 211, 546
Irwin, M., Tremaine, S., & Zytkow, A. N. 1995, AJ, 110, 3082
Ishiguro, M., Kuroda, D., Hasegawa, S., et al. 2014, ApJ, 792, 74
Jewitt, D., & Haghighipour, N. 2007, ARA&A, 45, 261
Johnson, T. V., & Lunine, J. I. 2005, Natur, 435, 69
Karkoschka, E. 2001, Icar, 151, 51
Lacerda, P., Fornasier, S., Lellouch, E., et al. 2014, ApJL, 793, L2
Laidler, V., et al. 2005, Synphot users guide, Version 5.0 (Baltimore, MD: STScI)
Li, J., A'Hearn, M. F., & McFadden, L. 2003, DPS Meeting, 35, 24.04
Li, J., A'Hearn, M. F., & McFadden, L. A. 2004, Icar, 172, 415
Li, J.-Y., Besse, S., A'Hearn, M. F., et al. 2013, Icar, 222, 559
Li, J.-Y., Schröder, S. E., Mottola, S., et al. 2019, Icar, 322, 144
Lomb, N. R. 1976, Ap&SS, 39, 447
Masoumzadeh, N., & Boehnhardt, H. 2019, Icar, 326, 1
Masoumzadeh, N., Boehnhardt, H., Li, J.-Y., & Vincent, J. B. 2015, Icar, 257, 239
McGuire, A. F., & Hapke, B. W. 1995, Icar, 113, 134
McLeod, B., Geary, J., Conroy, M., et al. 2015, PASP, 127, 366
Miller, C., Verbiscer, A. J., Chanover, N. J., Holtzman, J. A., & Helfenstein, P. 2011, Icar, 212, 819
Miyazaki, S., Komiyama, Y., Nakaya, H., et al. 2012, Proc. SPIE, 8446, 84460Z
Moore, J. M., McKinnon, W. B., Cruikshank, D. P., et al. 2018, GeoRL, 45, 8111
Muinonen, K. 1990, Light Scattering by Inhomogeneous Media: Backward Enhancement and Reversal of Linear Polarization (Helsinki: Helsinki Univ.)
National Research Council Solar System Exploration Survey 2003, New Frontiers in the Solar System: An Integrated Exploration Strategy (Washington, DC: National Academies Press)
Porter, S. B., Buie, M. W., Parker, A. H., et al. 2018, AJ, 156, 20
Porter, S. B., Spencer, J. R., Benecchi, S., et al. 2016, ApJL, 828, L15

Rabinowitz, D. L., Schaefer, B. E., & Tourtellotte, S. W. 2007, AJ, 133, 26
Scargle, J. D. 1982, ApJ, 263, 835
Schaefer, B. E., Rabinowitz, D. L., & Tourtellotte, S. W. 2009, AJ, 137 129
Shkuratov, I. G. 1988, KFNT, 4, 33
Simonelli, D. P., Kay, J., Adinolfi, D., et al. 1999, Icar, 138, 249
Simonelli, D. P., Wisz, M., Switala, A., et al. 1998, Icar, 131, 52
Spjuth, S., Jorda, L., Lamy, P. L., Keller, H. U., & Li, J. Y. 2012, Icar, 221, 1101
Stern, S. A., Bagenal, F., Ennico, K., et al. 2015, Sci, 350, aad1815
Stern, S. A., Weaver, H. A., Spencer, J. R., & Elliott, H. A. 2018, SSRv, 214, 77
Stern, S. A., Weaver, H. A., Spencer, J. R., et al. 2019, Sci, 364, aaw9771
Takir, D., Clark, B. E., Drouet d'Aubigny, C., et al. 2015, Icar, 252, 393
Tatsumi, E., Domingue, D., Hirata, N., et al. 2018, Icar, 311, 175
Thirouin, A., Ortiz, J. L., Duffard, R., et al. 2010, A&A, 522, A93
Thomas, P., Veverka, J., & Helfenstein, P. 1991, JGR, 96, 19253
Thomas, P. C., Adinolfi, D., Helfenstein, P., Simonelli, D., & Veverka, J. 1996, Icar, 123, 536
Verbiscer, A., French, R., Showalter, M., & Helfenstein, P. 2007, Sci, 315, 815
Verbiscer, A., & Helfenstein, P. 1998, in Solar System Ices, ed. B. Schmitt, C. de Bergh, & M. Festou (Dordrecht: Kluwer), 157
Verbiscer, A., Helfenstein, P., Buratti, B., & Royer, E. 2018a, in Enceladus and the Icy Moons of Saturn, ed. P. Schenk et al. (Tucson, AZ: Univ. Arizona Press), 323
Verbiscer, A. J., Helfenstein, P., & Buratti, B. J. 2013, in The Science of Solar System Ices, ed. M. S. Gudipati & J. Castillo-Rogez (New York: Springer), 47
Verbiscer, A. J., Porter, S. B., Buratti, B. J., et al. 2018b, ApJL, 852, L35
Verbiscer, A., Showalter, M. R., Buie, M. W., & Helfenstein, P. 2019, LPICo, 2133, 7050
Verbiscer, A. J., & Veverka, J. 1988, Icar, 73, 324
Verbiscer, A. J., & Veverka, J. 1990, Icar, 88, 418
Warell, J., & Bergfors, C. 2008, P&SS, 56, 1939